



# LZ-STAR Survey: Low-metallicity Star Formation Survey of Sh2-284. I. Ordered Massive Star Formation in the Outer Galaxy

Yu Cheng<sup>1,2</sup> , Jonathan C. Tan<sup>2,3</sup> , Morten Andersen<sup>4</sup> , Rubén Fedriani<sup>3,5</sup> , Yichen Zhang<sup>2,6</sup> , Massimo Robberto<sup>7</sup> ,  
Zhi-Yun Li<sup>2</sup> , and Kei E. I. Tanaka<sup>8</sup>

<sup>1</sup> National Astronomical Observatory of Japan, 2-21-1 Osawa, Mitaka, Tokyo 181-8588, Japan; [yucheng.astro@gmail.com](mailto:yucheng.astro@gmail.com)

<sup>2</sup> Department of Astronomy, University of Virginia, Charlottesville, VA 22904, USA

<sup>3</sup> Department of Space, Earth & Environment, Chalmers University of Technology, 412 93 Gothenburg, Sweden

<sup>4</sup> European Southern Observatory, Karl Schwarzschild Str. 2, 85748 Garching, Germany

<sup>5</sup> Instituto de Astrofísica de Andalucía, CSIC, Glorieta de la Astronomía s/n, 18008 Granada, Spain

<sup>6</sup> Department of Astronomy, School of Physics and Astronomy, Shanghai Jiao Tong University, 800 Dongchuan Rd., Minhang, Shanghai 200240, People's Republic of China

<sup>7</sup> Space Telescope Science Institute, 3700 San Martin Drive, Baltimore, MD 21218, USA

<sup>8</sup> Department of Earth and Planetary Sciences, Institute of Science Tokyo, Meguro, Tokyo 152-8551, Japan

Received 2025 March 18; revised 2025 May 30; accepted 2025 May 30; published 2025 September 10

## Abstract

Star formation is a fundamental, yet poorly understood, process of the Universe. It is important to study how star formation occurs in different galactic environments. Thus, here, in the first of a series of papers, we introduce the Low-metallicity Star Formation (LZ-STAR) survey of the Sh2-284 (hereafter S284) region, which, at  $Z \sim 0.3\text{--}0.5Z_{\odot}$ , is one of the lowest-metallicity star-forming regions of our Galaxy. LZ-STAR is a multifacility survey, including observations with JWST, the Atacama Large Millimeter/submillimeter Array (ALMA), Hubble Space Telescope, Chandra, and Gemini. As a starting point, we report JWST and ALMA observations of one of the most massive protostars in the region, S284p1. The observations of shock-excited molecular hydrogen reveal a symmetric, bipolar outflow originating from the protostar, spanning several parsecs, and fully covered by the JWST field of view and ALMA observations of CO(2–1) emission. These allow us to infer that the protostar has maintained a relatively stable orientation of disk accretion over its formation history. The JWST near-infrared continuum observations detect a centrally illuminated bipolar outflow cavity around the protostar, as well as a surrounding cluster of low-mass young stars. We develop new radiative transfer models of massive protostars designed for the low metallicity of S284. Fitting these models to the protostar's spectral energy distribution implies a current protostellar mass of  $\sim 10 M_{\odot}$  has formed from an initial  $\sim 100 M_{\odot}$  core over the last  $\sim 3 \times 10^5$  yr. Overall, these results indicate that massive stars can form in an ordered manner in low-metallicity, protocluster environments.

*Unified Astronomy Thesaurus concepts:* Jets (870); Star formation (1569); Metallicity (1031); Young stellar objects (1834); Massive stars (732)

## 1. Introduction

Star formation is a fundamental process for the cosmos with many open questions. To gain a comprehensive understanding, it is crucial to study star-forming clouds in a wide range of environments. Among various environmental factors, metallicity ( $Z$ ) stands out as a particularly interesting variable. Since cosmic metallicity increases in time with the evolution of the Universe, the formation of stars at low metallicities, especially the determination of their characteristic mass scales, is important for understanding properties of high-redshift galaxies and the early history of the Milky Way. Metallicity may affect star formation via influencing heating and cooling processes and the ionization fraction in molecular gas, which may then regulate collapse, fragmentation, and stellar feedback. For example, theoretical and observational studies indicate that metallicity may affect global star formation properties, including the stellar initial mass function (e.g., M. Marks et al. 2012; K. E. I. Tanaka et al. 2018; J. Li et al. 2023). The lifetimes of protoplanetary disks may also be

impacted by the metallicity of the environment (G. De Marchi et al. 2024).

Due to limitations in sensitivity and spatial resolution, observational studies capable of spatially resolving low-metallicity star-forming cores and the resulting young stellar populations have primarily focused on relatively nearby targets, such as the Large and Small Magellanic Clouds (LMC and SMC) and the extreme outer Galaxy (defined as regions with galactocentric distances greater than 18 kpc; C. Yasui et al. 2006). These regions, with subsolar metallicities of  $\approx 0.2\text{--}0.5Z_{\odot}$ , offer low-metallicity environments that may resemble those of high-redshift galaxies or the early Milky Way. With advancements in recent observational facilities, significant progress has been made. The unprecedented capabilities of the James Webb Space Telescope (JWST), for example, have enabled the detection of dusty, subsolar mass young stellar objects (YSOs) in the NGC 346 region of the SMC (O. C. Jones et al. 2023). C. Yasui et al. (2024) reported the detection of brown dwarfs and a mass function with a relatively low peak mass in the outer Galaxy region, Digel Cloud 2. For embedded YSOs still in their early stages of evolution, observations with interferometers such as the Atacama Large Millimeter/submillimeter Array (ALMA) have significantly advanced our understanding of the physical processes involved during massive star formation, including



Original content from this work may be used under the terms of the [Creative Commons Attribution 4.0 licence](https://creativecommons.org/licenses/by/4.0/). Any further distribution of this work must maintain attribution to the author(s) and the title of the work, journal citation and DOI.

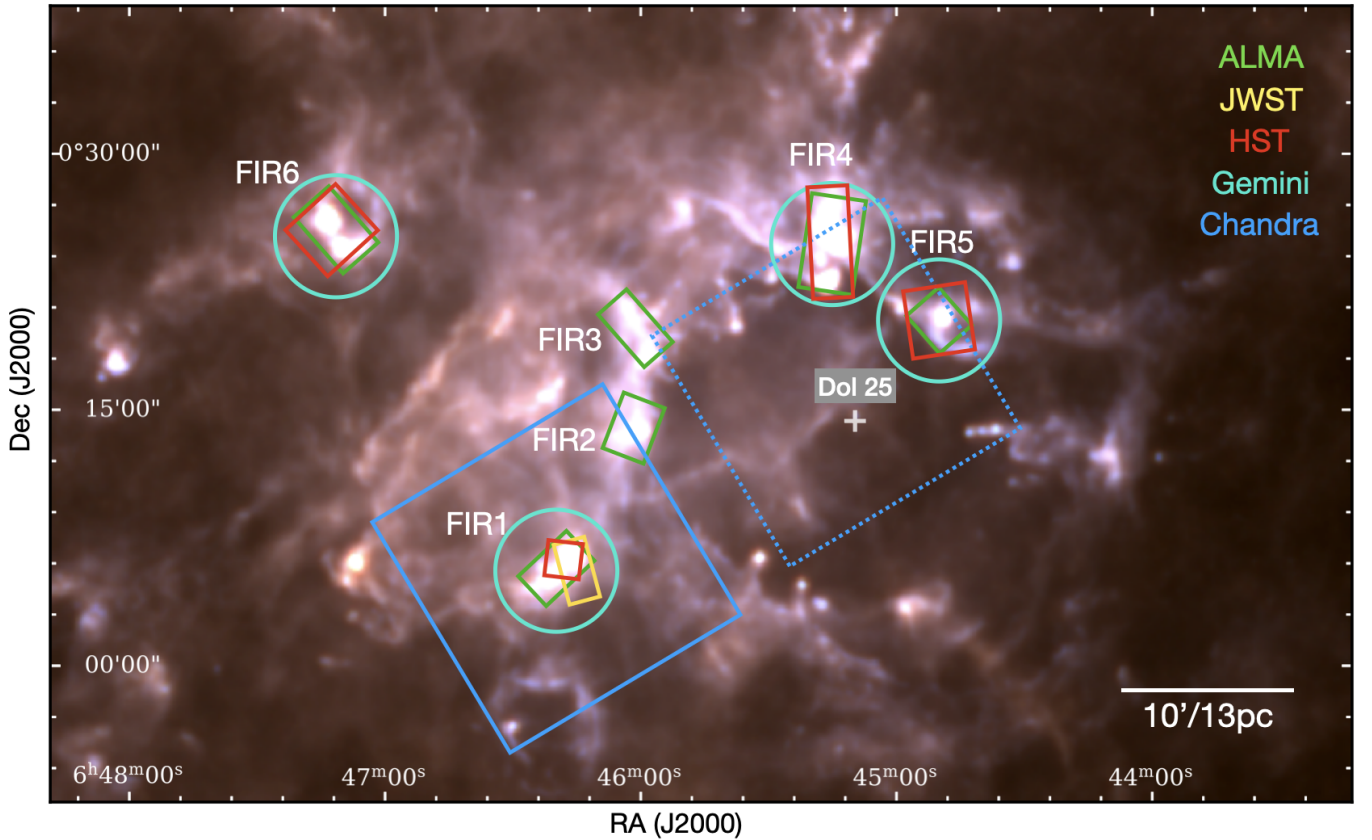


**Figure 1.** Color composite image of the S284 region constructed by combining Herschel 250  $\mu\text{m}$  (blue), 350  $\mu\text{m}$  (green), and 500  $\mu\text{m}$  (red) images. The colored rectangles or circles indicate the field of view (FOV) of our observations from different facilities including ALMA, JWST, the Hubble Space Telescope (HST), Gemini, and Chandra. For Chandra the FOV of an archival observation program targeting the Dolidze 25 cluster is also shown (dashed rectangle; M. G. Guarcello et al. 2021).

the characterization of filaments (K. Tokuda et al. 2023, 2025), chemically rich hot cores (T. Shimonishi et al. 2016, 2020, 2021, 2023), molecular outflows (Y. Fukui et al. 2015; K. Tokuda et al. 2022), and jets with associated rotating toroids (A. F. McLeod et al. 2018, 2024). These studies provide valuable insights into star formation in low-metallicity environments. However, a systematic investigation that combines the characterization of star-forming gas and the newly formed stellar content at low metallicity remains lacking.

### 1.1. LZ-STAR Survey Overview

To obtain a more comprehensive understanding of star formation in low-metallicity conditions, we have undertaken the Low-metallicity Star Formation (LZ-STAR) survey of Sh2-284 (Co-PIs: Y. Cheng and J. C. Tan). Initially identified as a diffuse nebula in the Sharpless catalog (S. Sharpless 1959), Sh2-284 (hereafter S284) is located in the outer Galaxy, approximately 4.5 kpc from the Sun (I. Negueruela et al. 2015). Spectroscopic observations of OB stars within S284 indicate a low metallicity, with abundances of 0.3 dex (Si) and 0.5 dex (O) below solar values (I. Negueruela et al. 2015), i.e., corresponding to metallicities of approximately one-third to one-half solar, which are comparable to those of the LMC. As such, S284 is one of the most metal-poor star-forming regions currently known in the Milky Way. In

addition, S284 is a large, active star-forming complex spanning at least 50 pc as projected on the sky. One of its main features is an H II region ionized by the young open cluster Dolidze 25. Surrounding the H II region are dense molecular clouds with ongoing active star formation (E. Puga et al. 2009).

Figure 1 shows a Herschel far-infrared (FIR) image of the S284 region, along with annotations of the various subregions that have been targeted in the LZ-STAR survey. The survey involves multiple facilities operating at different wavelengths to trace the star formation at different stages from the dense gas to already formed young stellar clusters. Here we give a brief overview of these observations, with most of the data and results to be presented in future papers in this series. We have identified six regions (S284-FIR1 to FIR6) in S284 with active star formation, as evidenced by the strong dust emission seen in Herschel images (Figure 1) and large numbers of young stars in previous infrared surveys (E. Puga et al. 2009; M. G. Guarcello et al. 2021).

ALMA observations were carried out toward S284-FIR1 to FIR6 in Cycles 8 and 11 in band 6 (1.3 mm), achieving a spatial resolution of  $0''.5$ – $1''.5$ . As described in more detail in Section 2, these observations are designed to detect millimeter continuum dust emission from dense cores, as well as molecular line emission from various species tracing both dense gas and protostellar outflows. Additional data from



APEX-nFlash230 and SEPIA345, and IRAM-30m-NIKA2 have also been obtained for one of the regions (S284-FIR1, see Figure 1) to provide dust continuum and gas kinematics on large scales.

To study the young stellar population, we have carried out near-infrared (NIR) observations with the Gemini-South, HST, and JWST. JWST Near-Infrared Camera (NIRCam) observations have been obtained for one region (S284-FIR1), described in more detail in Section 2, using six filters from 1.6 to 4.7  $\mu\text{m}$  designed to detect continuum emission, as well as Br $\alpha$  and excited H $_2$  emission. HST/WFC3/IR observations in the F125W, F139M, and F160W filters (Cycle 21), cover four of the six regions (FIR1, FIR4, FIR5, and FIR6) with the primary goal of characterizing YSO properties. Similarly, Gemini-South observations with Flamings-2 in the *J*, *H*, and *Ks* filters also cover these four regions and are also sensitive to YSOs. In addition, Chandra ACIS-I observations (Cycle 23, 270 ks) have also been obtained to facilitate identification of pre-main-sequence stars in a  $17' \times 17'$  FOV centered on S284-FIR1.

In this paper, the first of a series presenting results from the LZ-STAR survey, we present ALMA band 6 and JWST/NIRCam observations toward the dense clump S284-FIR1 and report a candidate massive protostellar object with its outflow structure well resolved in both CO and the H $_2$  4.7  $\mu\text{m}$  line. The structure of this paper is as follows: the observations are described in Section 2; the results are presented in Section 3; the implications of these results are discussed in Section 4; and a summary is given in Section 5.

## 2. Observations

### 2.1. ALMA Observations

The ALMA observations of S284-FIR1 were conducted in band 6 in Cycle 8 (Project ID 2021.1.01706.S, PI: Y. Cheng), during the period from 2021 November to 2022 May. We divided the entire survey field ( $5''.5 \times 3'$ ) into three strips, each about  $3'$  long and  $1''.8$  wide. We employed the compact configuration C43-3 to recover scales between  $0''.6$  and  $7''$ . Additionally, a 7 m array mosaic was performed for each strip, probing scales up to  $29''$ . Total-power observations of the region were also carried out. We set the central frequency of the correlator sidebands to be the rest frequency of the N $_2\text{D}^+(3-2)$  line at 231.32 GHz for spectral window (SPW) zero with a velocity resolution of  $0.046 \text{ km s}^{-1}$ . The second baseband SPW1 was set to 231.00 GHz, i.e., 1.30 mm, to observe the continuum with a total bandwidth of 1.875 GHz, which also covers CO(2–1) with a velocity resolution of  $1.46 \text{ km s}^{-1}$ . SPW2 was split to cover the  $^{13}\text{CO}(2-1)$  and C $^{18}\text{O}(2-1)$  lines, both with a velocity resolution of  $0.096 \text{ km s}^{-1}$ . The frequency coverage for SPW3 ranged from 215.85 to 217.54 GHz to observe DCN(3–2), DCO $^+(3-2)$ , SiO(5–4), and CH $_3\text{OH}(5_{1,4}-4_{2,2})$ .

The raw data were calibrated with the data reduction pipeline using CASA 6.2.1. The continuum visibility data were constructed with all line-free channels. We performed imaging with the `tclean` task in CASA and during cleaning we combined data for all three strips to generate a final mosaic map. The combined 12 m array and 7 m array data were imaged using a Briggs weighting scheme with a robust parameter of 0.5, which yields a resolution of  $0''.64 \times 0''.54$  for the continuum. The  $1\sigma$  noise levels in the continuum image are  $0.11 \text{ mJy beam}^{-1}$ . We feathered the line

images with the total-power images to correct for the missing large-scale structures. In this paper we mainly focus on the CO(2–1) line, which has a spatial resolution of  $0''.74 \times 0''.64$  and a sensitivity of  $3.5 \text{ mJy beam}^{-1}$  per  $1.5 \text{ km s}^{-1}$  channel.

### 2.2. JWST Observations

JWST observations of S284-FIR1 were conducted on 2022 October 19 with NIRCam (M. J. Rieke et al. 2005; C. A. Beichman et al. 2012) using the F162M, F182M, F200W, F356W, F405N, and F470N filters (GO:2317, PI: Y. Cheng), available at MAST at doi:10.17909/5ne9-9e82. The brightest part of FIR1 was centered in one of the CCDs of NIRCam and, to ease scheduling, the orientation was left unconstrained. This ultimately yielded partial overlap with the ALMA FOV (see Figure 1). The exposure time for the six filters were 1739 s, 1739 s, 644 s, 644 s, 1739 s, and 1739 s, respectively. The observations were performed adopting a Fullbox3 tight dither pattern as well as two subpixel dithers, to cover a field of approximately  $5' \times 2'$ . The 6.5 m diameter of JWST gives an angular resolution of  $\sim 0''.07$ – $0''.17$  over the range of NIRCam wavelengths in this study. The NIRCam images were rereduced using the JWST Calibration Pipeline version 1.12.5 (H. Bushouse et al. 2023). The three short-wavelength (SW) filters were reduced using a single pixel scale of  $0''.03$  and the first read was used for increased dynamic range. The long-wavelength module was reduced in a similar manner, but with a pixel scale of  $0''.06$ .

## 3. Results

### 3.1. Star Formation in S284-FIR1

S284-FIR1 is one of the most active star-forming regions in S284. It contains a parsec-scale main clump and an extension of dense gas to the SE. From a 2D gaussian fit to the Herschel Hi-GAL FIR dust emission derived column density map (S. Molinari et al. 2010), we estimate the clump has a FWHM of about  $30''$  ( $0.65 \text{ pc}$ ) and a dust mass of  $2.7 M_\odot$ . To estimate the total gas mass, we adopt a metallicity of  $-0.3 \text{ dex}$  (I. Negueruela et al. 2015), i.e.,  $0.5Z_\odot$ . Scaling the local Galactic refractory dust-to-gas mass value of 141 (B. T. Draine 2011) for this metallicity yields a ratio of 282 and a total gas mass of about  $760 M_\odot$ . Thus the mass surface density of the clump averaged inside the half-mass radius is  $\Sigma_{\text{cl}} = 0.15 \text{ g cm}^{-2}$ . Such clump mass surface densities are known to be sufficient to form massive stars in more typical, higher-metallicity regions of the Galaxy (J. M. De Buizer et al. 2017; M. Liu et al. 2019, 2020; R. Fedriani et al. 2023; Z. Telkamp et al. 2025).

#### 3.1.1. ALMA 1.3 mm Continuum

Figure 2 presents the ALMA 1.3 mm dust continuum map of S284-FIR1 with a resolution of  $0''.64 \times 0''.54$  ( $2870 \text{ au} \times 2430 \text{ au}$ ). The image reveals compact sources that are sparsely distributed over the FOV. We identify cores using the `astrodendro` algorithm (E. W. Rosolowsky et al. 2008) using parameters of a  $4\sigma$  threshold,  $1\sigma$  minimum step, and minimum core area of half a beam. These choices represent a reasonable compromise between completeness and the robustness of source identification (e.g., Y. Cheng et al. 2018); this set of parameters is also adopted in a series of core mass function (CMF) studies by Y. Cheng et al. (2018), M. Liu et al. (2018),

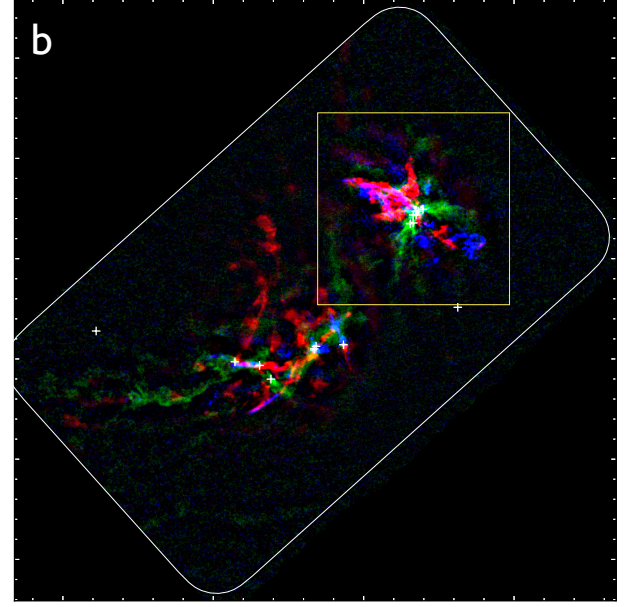
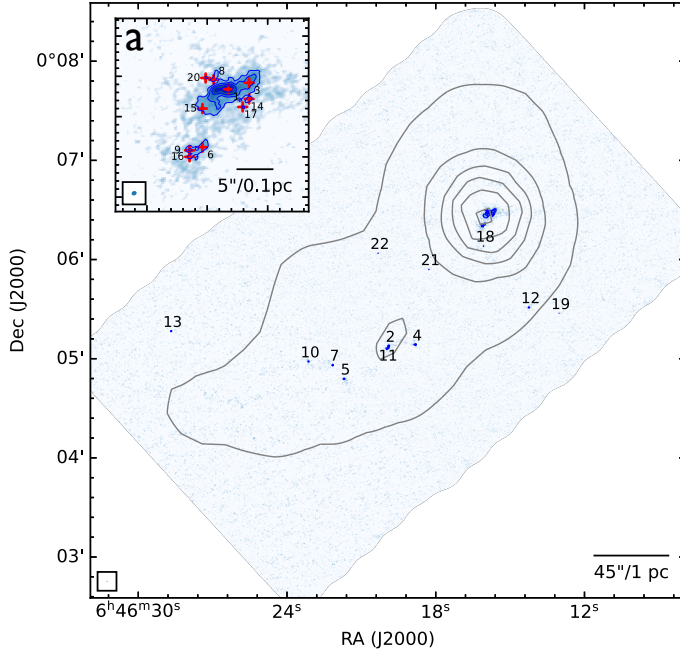


**Figure 2.** (a) ALMA band 6 (1.3 mm) continuum of the S284-FIR1 region shown in blue color scale and contours. The contour levels are  $0.11 \text{ mJy beam}^{-1} \times (5, 10, 20, 40, 80)$ . We overlay the Herschel  $500 \mu\text{m}$  image in gray contours for comparison. The identified cores are numbered. A zoom-in view is shown in the top left corner, where the red crosses denote the positions of identified dense cores. (b) Three-color image made with ALMA data in the same FOV as (a), where green is  $\text{C}^{18}\text{O}(2-1)$  emission integrated over  $-5$  to  $5 \text{ km s}^{-1}$  relative to the systemic velocity; and blue/red is  $\text{CO}(2-1)$  integrated from  $5$  to  $10 \text{ km s}^{-1}$  blue-/redshifted relative to the systemic velocity. The yellow box indicates the position of the main outflow discussed in this work, which is further shown in Figure 5.

T. J. O’Neill et al. (2021), and A. V. I. Kinman et al. (2025). We note that cores are identified in the ALMA images before any primary beam correction is applied, which allows a uniform noise level. Then final flux and mass estimates are adjusted to account for the primary beam correction, which is relevant near the edge of the mosaic regions.

The cores are labeled in Figure 2(a). We estimate core gas masses by assuming their emission arises from optically thin isothermal dust, i.e.,

$$M_{\text{gas}} = R_{\text{gd}} \frac{d^2 F_{\nu}}{\kappa_{\nu} B_{\nu}(T_d)}, \quad (1)$$

where  $d$  is the distance,  $R_{\text{gd}}$  is the gas-to-dust mass ratio,  $F_{\nu}$  is the observed flux density,  $B_{\nu}$  is the Planck function,  $T_d$  is the dust temperature and  $\kappa_{\nu}$  is the dust opacity at the observed wavelength. Following Y. Cheng et al. (2018), we assume a uniform dust temperature of 20 K and adopt  $\kappa_{1.3\text{mm}} = 0.899 \text{ cm}^2 \text{ g}^{-1}$  (i.e., from the moderately coagulated thin ice mantle model of V. Ossenkopf & T. Henning 1994). We also adopt  $R_{\text{gd}} = 282$ , as discussed above.

With the above assumptions, the identified cores have masses ranging from  $0.37 M_{\odot}$  to  $68.2 M_{\odot}$ . If temperatures of 10 K or 30 K were to be adopted, then the mass estimates would differ by factors of 1.85 and 0.677, respectively. Thus we see that relatively massive cores are present, which have the potential to form massive stars. In Figure 3, we present the CMF derived from the observed core sample. Due to the limited number of cores, the functional form of the distribution is not well constrained. We expect that incorporating additional ALMA observations from other regions in S284 in future work will improve these constraints. Also note that

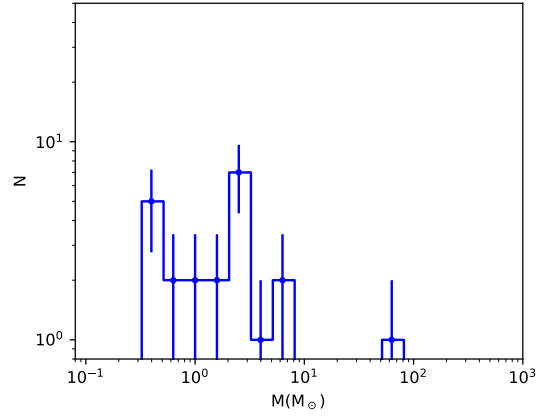


**Figure 3.** The mass distribution of cores detected in the S284-FIR1 region.

the flux densities and areas returned by the dendrogram may be underestimated due to isophotal cutoffs, and require further correction before being used for assessing the cumulative properties of the core sample (e.g., A. V. I. Kinman et al. 2025).

From examination of the ALMA data tracing high-velocity (both blue- and redshifted)  $\text{CO}(2-1)$  emission (Figure 2(b)), we see that most of these cores are associated with molecular outflows, often exhibiting highly collimated morphologies. This confirms the presence of active and widespread star formation in S284-FIR1. Among the detected outflows, the most prominent one appears to be driven by a source near the center of the main clump in S284-FIR1 (shown in the yellow box in Figure 2). It extends several parsecs along the NE–SW

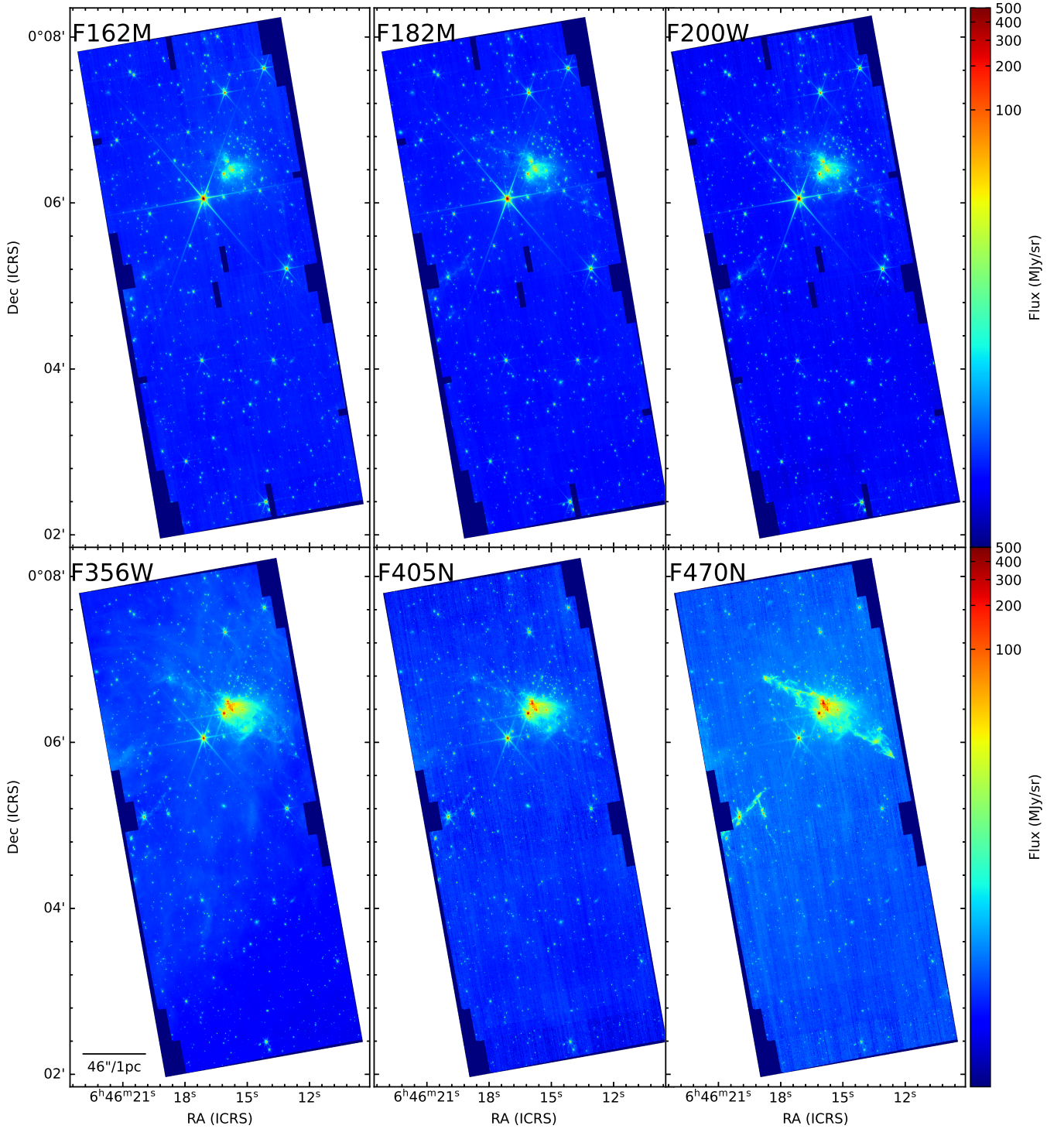


**Figure 4.** JWST images in six filters (F162M, F182M, F200W, F356W, F405N, and F470N) toward the S284-FIR1 region.

axis. This outflow is mostly likely associated with a massive protostar, which we refer to as S284p1.

### 3.1.2. JWST Images

In Figure 4, we present JWST images in all six observed filters toward S284-FIR1. The images reveal a cluster of approximately 200 stars in the northern part of the FOV, coinciding with the main clump in S284-FIR1. Analysis of the colors and fluxes of these stars indicates that they are embedded, recently formed YSOs (M. Andersen et al. 2025,

in preparation), with a significant fraction exhibiting infrared excess (A. Brizawasi et al. 2025, in preparation). A prominent IR continuum reflection nebula is visible, particularly at longer wavelengths (F356W, F405N, and F470N), powered by sources near the cluster center and extending to the SW. Additionally, the F470N image, which traces the  $\text{H}_2$  4.7  $\mu\text{m}$  line, reveals a large bipolar jet ejected from the cluster center. This emission line corresponds to the pure rotational transition  $\text{H}_2(0-0 \text{ S}(9))$ , with an upper state energy level of 10,263 K, making it an excellent tracer of shocks in jets and outflows



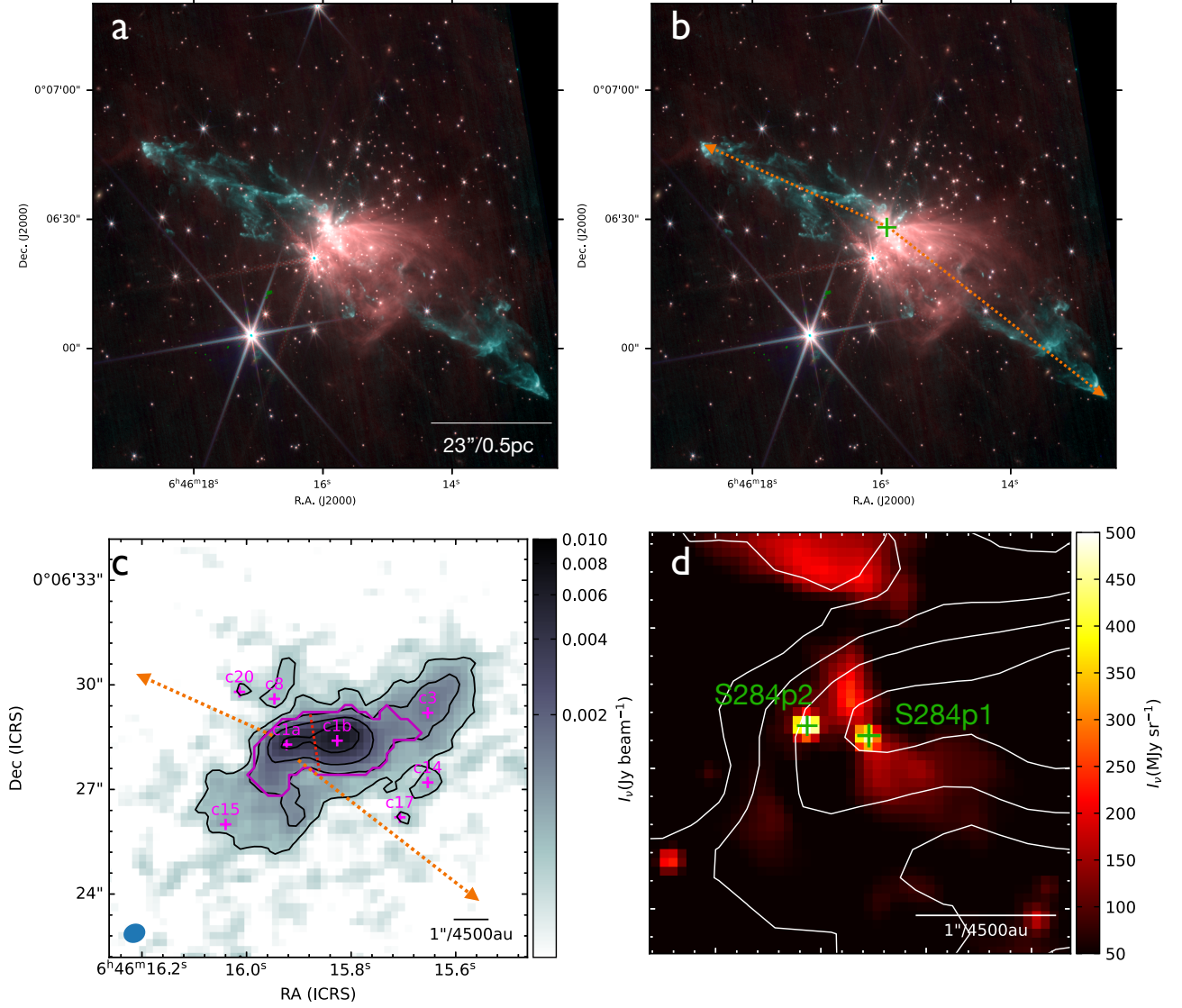


**Figure 5.** Overview of the massive protostar S284p1 and its outflow. (a) JWST color composite image with  $1.62\ \mu\text{m}$ ,  $2.0\ \mu\text{m}$ ,  $3.56\ \mu\text{m}$ , and  $4.70\ \mu\text{m}$  in blue, green, red, and cyan, respectively, and with the latter highlighting excited  $\text{H}_2$  emission. (b) Same as (a). The green cross indicates the position of S284p1 and the orange dashed arrows show the connection between S284p1 and the outflow termination shocks. (c) Zoom-in view of S284p1 in 1.3 mm (ALMA) continuum emission (contour levels of 5, 10, 20, 40, and  $80 \times 0.11\ \text{mJy beam}^{-1}$ ). The magenta crosses indicate the positions of identified dense cores. The dashed arrows indicate the orientation of the outflows as in (b). The magenta contour highlights the core boundary for c1 returned by *astrodendro*. We manually separate the two peaks (c1a and c1b) in c1, with the boundary shown by the dashed red line. (d) A further zoom-in view of S284p1, now showing the F356W image. The ALMA 1.3 mm continuum emission is shown with the same contours as in (c).

(J. Turner et al. 1977). Toward the eastern middle of the F470N FOV, at least two additional collimated jets are visible, which are also detected in the CO data. Some jets or jet knots are also seen in other filters, including wide- and medium-band filters, which are likely partly contributed by molecular hydrogen lines within their frequency ranges.

### 3.2. The Massive Protostar S284p1

#### 3.2.1. Location of the Protostar and its Immediate Environment

A prominent outflow is identified in both CO(2–1) and  $\text{H}_2(0-0\ \text{S}(9))$ , which appears to be driven by a source near the center of the main parsec-scale clump in S284-FIR1. This is further illustrated in Figure 5(a), where we present a JWST color composite image combining the F162M, F200W, F356W, and F470N bands, represented in red, green, blue, and cyan

colors, respectively. The F470N ( $\text{H}_2\ 4.7\ \mu\text{m}$  line) emission highlights a protostellar outflow matching the basic orientation traced by the primary CO(2–1) outflow. The outflow extends about  $2'$  ( $\sim 2.6\ \text{pc}$ ) on the sky and contains numerous knots, arcs, and more diffuse emission features. This is among the longest outflow structures associated with a massive protostar ever observed via molecular hydrogen (e.g., J. Bally 2016). The large spatial extent and symmetric appearance of the jet suggest that the protostar has maintained a steady orientation throughout the majority of its formation history. The global geometry of the outflow, defined by the directions from the driving source to the termination bow shocks, is highlighted in Figure 5(b) and discussed in more detail below.

The driving source (S284p1) can be identified from the 1.3 mm continuum map as well as the JWST images. Figure 5(c) shows a zoom-in view of the ALMA 1.3 mm continuum

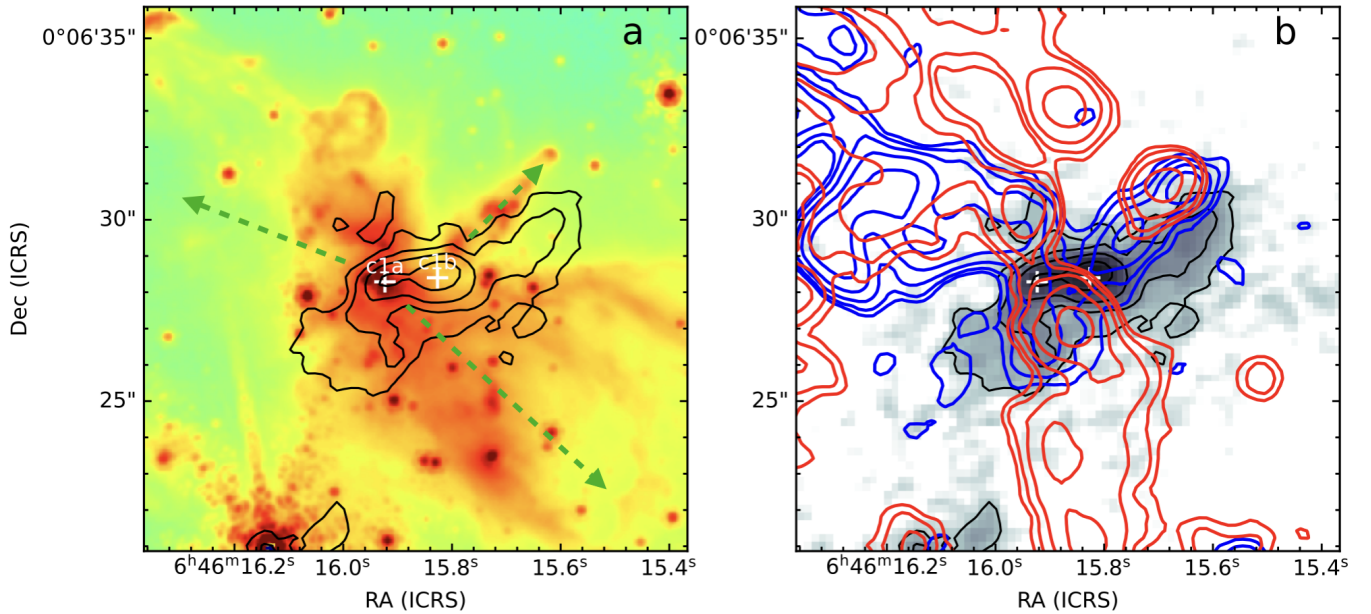


**Figure 6.** Zoom-in to outflow structures from S284p1. (a) F470N image in color scale with 1.3 mm continuum overlaid in contours. The white crosses denote the position for the two peaks in core c1. The dashed green arrows show the orientation of the outflows ejected from c1a and c1b. (b) Integrated CO(2–1) high-velocity emission in blue and red contours with 1.3 mm continuum overlaid in color scale and contours. The CO emission is integrated from 5 to 10 km s<sup>−1</sup> blue-/redshifted relative to the systemic velocity. The contour levels are 0.01 Jy beam<sup>−1</sup> km s<sup>−1</sup> × (5, 10, 20, 40, 80, and 160).

emission near the center of S284-FIR1. This image reveals seven dense cores within the clump, among which c1 has the highest millimeter flux densities and an estimated gas mass of  $68.2 M_{\odot}$  assuming a temperature of 20 K. A close inspection of the image shows that c1 is fragmented into two peaks separated by  $\sim 5000$  au. These are not identified by *astro-dendro* as two separate cores since they do not reach the minimum delta value ( $1\sigma$ ) threshold. However, since the protostar (S284p1, identified from the JWST F356W image, as will be discussed below) appears to be located at the position of the eastern peak (c1a), we manually divide c1 with the dividing line drawn along the emission minimum ridge. c1a is estimated to have a gas mass of  $20.7 M_{\odot}$ , while c1b has a mass of  $47.5 M_{\odot}$ . Based on the morphology of the H<sub>2</sub> 4.7  $\mu$ m and CO(2–1) integrated intensity maps (Figure 6), we identify c1a as the host for the driving source for the large-scale bipolar outflow. We also note that c1b hosts another protostar that drives another collimated outflow also seen in CO and H<sub>2</sub>, which is approximately orthogonal to the main outflow from c1a. This outflow exhibits a single-lobed and collimated appearance, extending to the NW direction from c1b. Given the overlapping blue- and redshifted high-velocity CO emission (Figure 6), we expect this outflow to be oriented close to the plane of sky. Therefore, its small extent likely indicates the protostar hosted by c1b is still in an early evolutionary stage.

The JWST/NIRCam data further reveal the NIR counterparts of the dense cores (Figures 5(d), 6(a), and 7). While c1b appears to have most of its NIR emission blocked by high extinction, c1a (i.e., S284p1) is clearly visible at 3.56  $\mu$ m and longer wavelengths (i.e., in the F356W, F405N, and F470N images). S284p1 is best resolved in the F356W band, which reveals a point source from the protostellar object surrounded by cone-like emission. Such morphology is expected for an

outflow cavity centrally illuminated by a massive protostar. Thus much of the observed F356W continuum emission is mostly likely dominated by scattered light emerging from outflow cavities, similar to morphologies observed around some lower-mass protostars (e.g., S. A. Federman et al. 2024). This cone-shaped emission extends approximately  $0^{\circ}5$  ( $\sim 2250$  au) on both sides of the protostar, with a half-opening angle of  $\sim 25^{\circ}$ . The orientation of the cone is broadly consistent with that of the main outflow axis. The NE outflow cone is significantly brighter than the SW cone, which suggests that the NE outflow is oriented toward our line of sight. This is consistent with there being a greater amount of blueshifted CO(2–1) emission on the NE side than on the SW side (see Figure 6(b)), although some blue- and redshifted emission is present on both sides, indicating a wide opening angle of the outflow (see also Figure 2(b)). For the narrowband F405N and F470N images, significant emission enhancement is clearly visible around the protostar but the cone morphology is less clear. We performed continuum subtraction but did not find clear evidence for line-emitting structures near the protostar (see Appendix A).

In all NIRCam bands there exists another illuminated feature about  $1''$  to the north of c1a, which also has a cone-like shape and shows similar morphology as the low-level 1.3 mm emission. It is possible that this is an IR reflection nebula that is illuminated by c1a or another source in the region. There is additional IR nebulosity to the south and east of c1a, where several point sources, likely to be YSOs, are also seen. The most prominent of these points sources, which we label S284p2, is approximately 3000 au to the east of S284p1 (see Figure 5(d)). Given its spectral energy distribution (SED), we consider that S284p2 is likely to be an embedded intermediate-mass YSO based (see Section 3.2.2).

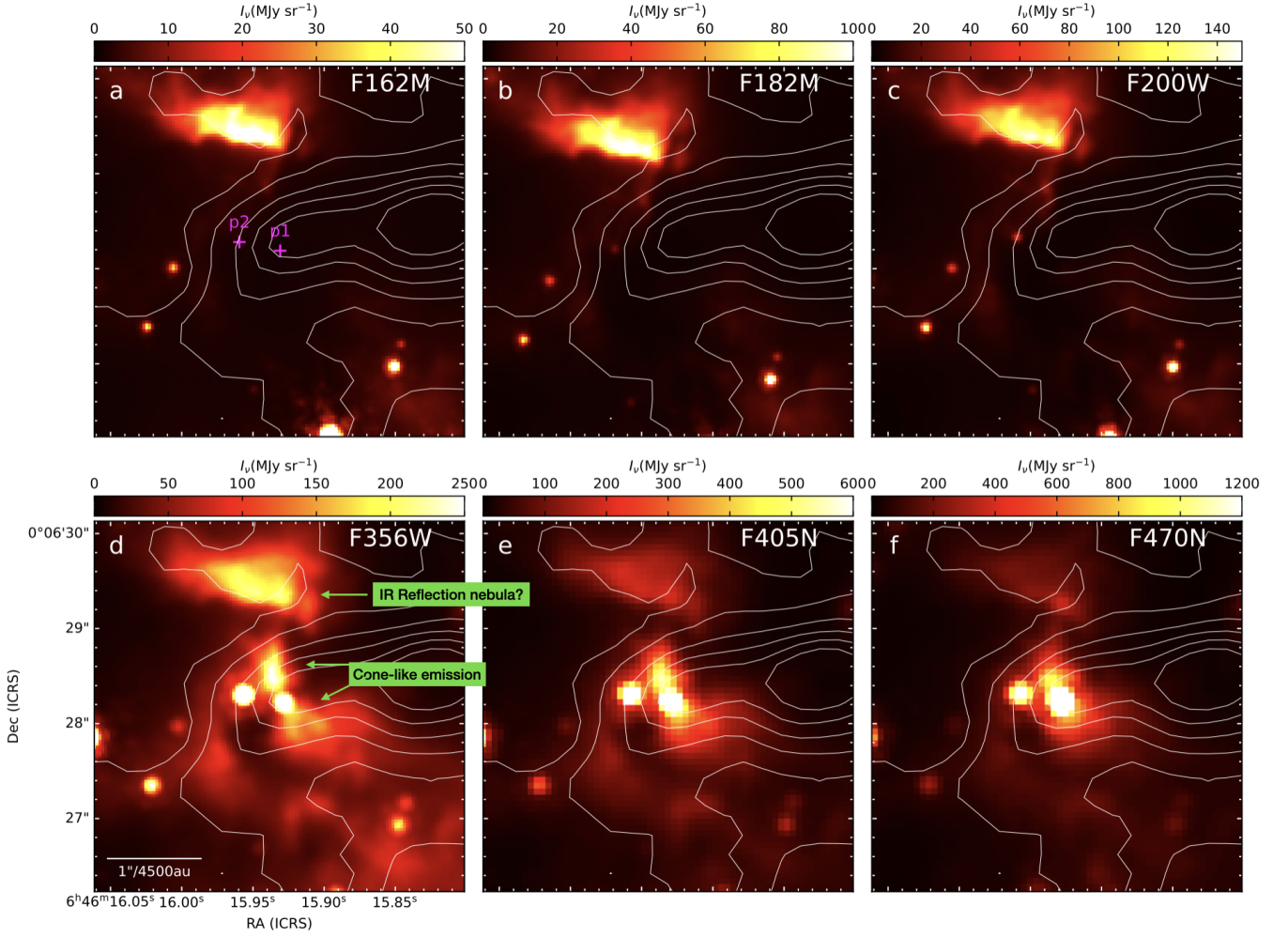


**Figure 7.** A zoom-in view of the NIR emission surrounding the massive protostar S284p1. (a) NIRCAM F162M band image in color scale overlaid with 1.3 mm continuum in contours. The contours levels are (5, 10, 20, 30, 40, and 50)  $\times 1.1$  Jy beam $^{-1}$ . The magenta crosses show the positions of the protostars S284p1 and S284p2. (b) Same as (a) but for F182M. (c) Same as (a) but for F200W. (d) Same as (a) but for F356W. (e) Same as (a) but for F405N. (f) Same as (a) but for F470N.

### 3.2.2. Properties of S284p1 from Spectral Energy Distribution Fitting

To determine the properties of the protostar S284p1, we performed an SED analysis. In addition to the JWST/NIRCAM data, we also retrieved the following archival data sets: Spitzer 3.5, 4.5, 5.8, and 8.0  $\mu$ m; Wide-field Infrared Survey Explorer (WISE) 12 and 22  $\mu$ m; and Herschel 70, 160, 250, 350, and 500  $\mu$ m (see Figure 8). We conduct the SED analysis following the methods of R. Fedriani et al. (2023), which is based on radiative transfer (RT) models developed within the framework of turbulent core accretion theory (Y. Zhang & J. C. Tan 2018, hereafter ZT18) and implemented with the Python package *sedcreator*. This method has been previously applied to Galactic high- and intermediate-mass protostars in a wide range of environments (e.g., J. M. De Buizer et al. 2017; M. Liu et al. 2019, 2020; R. Fedriani et al. 2023; Z. Telkamp et al. 2025).

The three primary physical parameters of the protostellar model grid are the initial mass of the core ( $M_c$ ), the mass surface density of the clump environment that the core is embedded in ( $\Sigma_{cl}$ ), and the current protostellar mass ( $m_*$ ), which describes the evolutionary state of a given core. Then the two remaining secondary parameters are the angle of the

line of sight to the outflow axis ( $\theta_{view}$ ) and the level of foreground extinction ( $A_V$ ). Other model parameters, such as initial core radius ( $R_{core}$ ), remaining core envelope mass ( $M_{env}$ ), and protostellar accretion rate ( $\dot{m}_*$ ) are specified by the three primary parameters.

To account for the low-metallicity condition of the region, we have computed a new grid of RT models scaling the opacity per unit gas down by a factor of two compared the ZT18 models. These models, to be presented separately in a future paper (Y. Zhang & J. C. Tan 2025, in preparation), are designed to represent massive protostars forming under half-solar-metallicity conditions. Below we investigate the systematic differences that arise in the SED fitting process from using the solar and half-solar-metallicity grid.

As input for the SED fitting we perform aperture photometry with a fiducial 15'' radius aperture. This radius was defined with the automated method based on the radial gradient of the background-subtracted enclosed flux at 70  $\mu$ m (R. Fedriani et al. 2023). We will consider cases where this fixed aperture is used at all wavelengths, which was the standard method of (R. Fedriani et al. 2023). However, we will also consider a case where at shorter wavelengths (i.e., probed



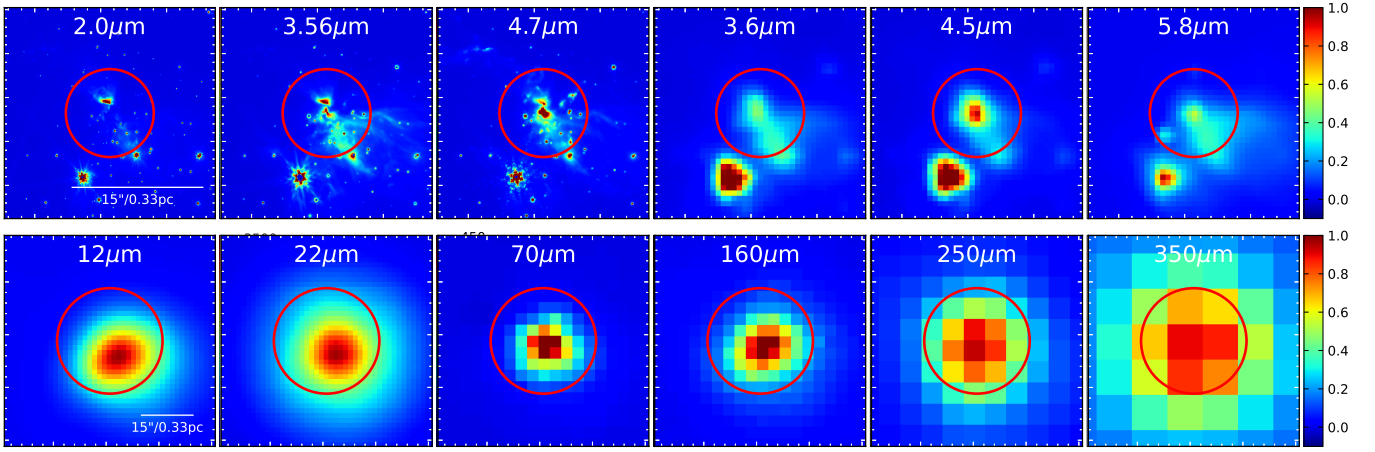


**Figure 8.** Maps of S284c1 at different wavelengths observed with JWST, Spitzer, WISE, and Herschel. The red circle in each panel indicates the aperture used for photometry for the fiducial SED analysis. These apertures have a radius of  $15''$  for wavelengths  $> 10 \mu\text{m}$  and  $5''$  for shorter wavelengths.

by the NIRCcam data, i.e.,  $< 5 \mu\text{m}$ ), a smaller aperture of  $5''$  radius is selected to avoid contamination from other sources.

We note that a major assumption of the SED fitting method is that a single protostar dominates the flux of the SED at each wavelength. In the case that other, secondary sources contribute significantly, then the derived bolometric luminosity and other related properties, such as current protostellar mass, should be regarded as upper limit constraints on the true source properties. In the case of S284p1, there are a number of factors that suggest the assumption of a single, dominant protostellar outflow from the region, as traced by both excited  $\text{H}_2$  emission and high-velocity CO emission. As discussed in Section 3.2.1, the next most significant outflow from the local vicinity appears to be driven from the core c1b, but the extent of this outflow (see Figure 6) is only  $\sim 4''$ , i.e., at least 10 times smaller than the outflow from S284p1. Nevertheless, below we will consider the impact on our results for S284p1 if c1b contributed 50% of the total flux. Next, the morphology of the source at FIR wavelengths near the peak of the SED, i.e., at  $70 \mu\text{m}$  is spatially concentrated and centered on the location of S284p1. Thus, we do not expect significant contributions to the FIR SED from sources in the more extended cluster. However, as noted, at shorter wavelengths, i.e.,  $< 5 \mu\text{m}$ , secondary sources can become more important, which then motivates their exclusion via use of a smaller aperture around the main source S284p1.

In terms of estimating the uncertainties associated with the flux measurements we first present cases that follow the methods of R. Fedriani et al. (2023). However, in the previous SED fitting analyses, data points at wavelengths  $\leq 10 \mu\text{m}$  were treated simply as upper limits, since the RT models do not include polycyclic aromatic hydrocarbon (PAH) emission or thermal emission from transiently heated small grains. To make better use of the JWST/NIRCcam fluxes, we also explore an option for using the JWST data points as valid measurements, instead of upper limits, but allowing an additional 50% systematic uncertainty to account for the PAH and small dust grain emission.

In summary, to investigate the sensitivity of the results to the choice of SED fitting method, we examine three cases.

1. *Case 1.* The standard method in R. Fedriani et al. (2023), i.e., using the Spitzer, WISE, and Herschel data with the solar-metallicity model grid. Here the Spitzer flux densities are included as upper limits.
2. *Case 2.* Same as Case 1 but using the  $0.5Z_\odot$  metallicity model grids.
3. *Case 3 (the fiducial case).* Same as Case 2, but including the JWST data. The flux densities in the F356W, F405N, and F470N bands are measured with an aperture of  $5''$  to exclude flux contributions from resolved secondary sources. In addition, these fluxes are now treated as measurements, rather than upper limits. To account for the uncertainties introduced due to PAH emission and emission from small dust grains, we add in quadrature an extra 50% systematic uncertainty. The Spitzer data at similar wavelengths are not included in the fit.

In Figure 9 we show the observed SED of S284p1 (panel (a)), followed by the SED fitting results of Cases 1, 2, and 3 (panels (b), (c), and (d), respectively). For the selection of acceptable, i.e., “good,” models, we follow the methods of Z. Telkamp et al. (2025). These are models that satisfy  $\chi^2 < 2$  (or the 10 best physical models if  $\chi^2_{\min} > 2$ ), where  $\chi^2_{\min}$  is the minimum value of the  $\chi^2$  statistic obtained across all models. The average and dispersion of the parameters of all “good” RT models are listed in Table 1.

For the fiducial Case 3, we derive a current protostellar mass of  $m_* = 10.2^{+3.9}_{-2.8} M_\odot$ , forming from a core with initial mass of  $M_c \sim 110 M_\odot$  that was embedded in a clump environment with a mass surface density of  $\Sigma_{\text{cl}} = 0.10^{+0.01}_{-0.01} \text{ g cm}^{-2}$ . The protostar is estimated to be accreting at a rate of  $\dot{m}_* = 6.0^{+0.6}_{-0.6} \times 10^{-5} M_\odot \text{ yr}^{-1}$ , while the current core envelope mass is  $M_{\text{env}} \sim 80 M_\odot$ . The bolometric luminosity of the source is  $\sim 1.5 \times 10^4 L_\odot$  and the age of the system is  $t_{\text{age}} \sim 3 \times 10^5 \text{ yr}$ .

We see that several of the derived parameters align well with other observational constraints. For example, the estimate of the current envelope mass agrees well with the mass of core c1, which we estimated from the ALMA 1.3 mm flux to have a mass of  $68 M_\odot$  (but based on the uncertain assumption of a dust temperature of 20 K). We note that given the aperture radius of  $15''$  used for SED fitting at longer wavelengths, this mass estimate includes the entire c1 core. Thus, protostellar

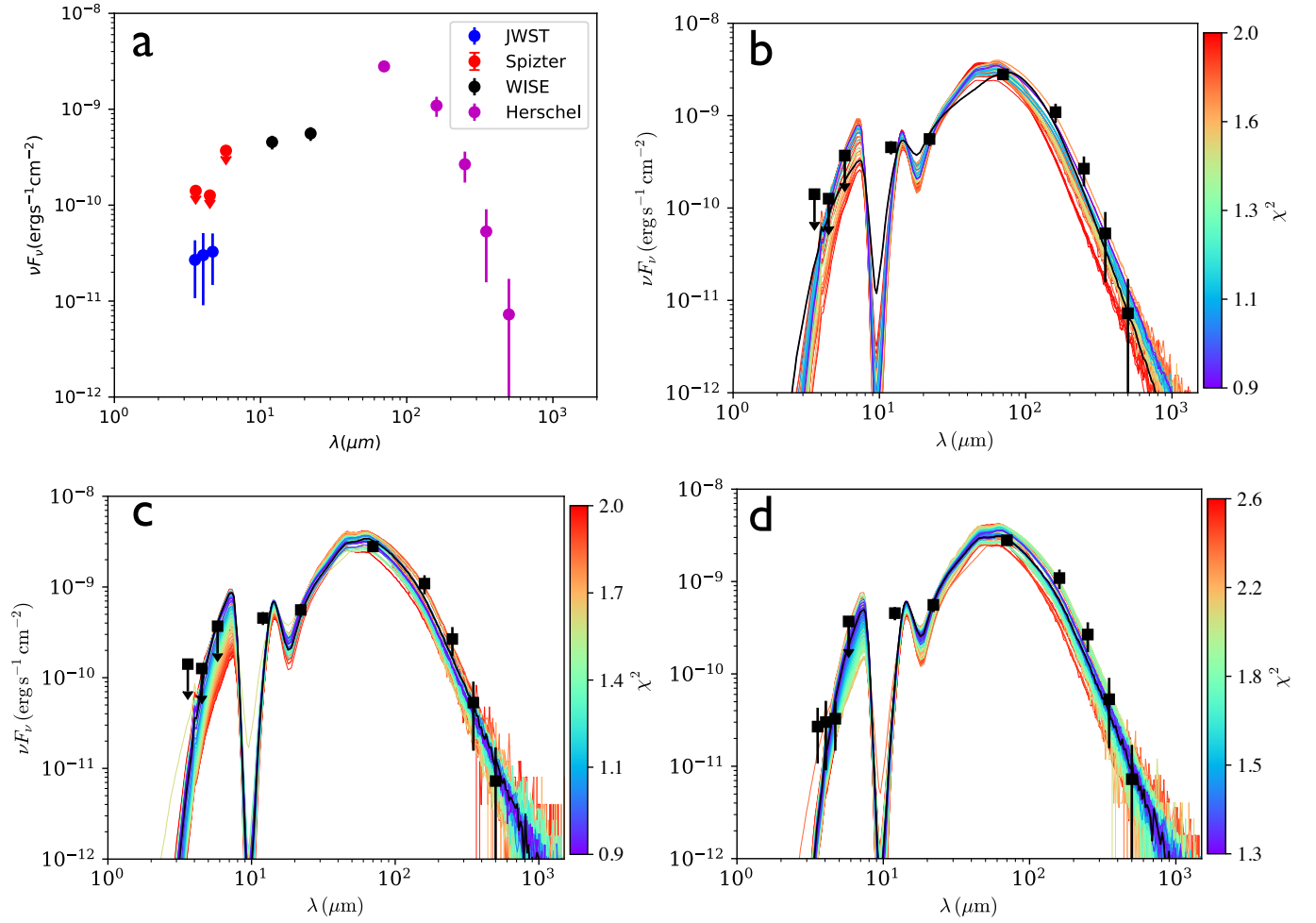


**Figure 9.** (a) Protostellar SEDs with fluxes that define the SED for S284p1, with telescope facilities labeled in the legend. (b)–(d) The SED fitting results for S284p1 with different fitting setups. The best-fitting protostar model is shown with a black line, while all other “good” model fits (see text) are shown with colored lines (red to blue with increasing  $\chi^2$ ). (b) Case 1: fitting uses Spitzer, WISE, and Herschel data with solar-metallicity model grids following method of R. Fedriani et al. (2023). (c) Case 2: same as (b), but using the half-solar-metallicity model grids. (d) Case 3: same as (c), but now fits include JWST/NIRCam data.

properties of initial core mass and current envelope mass that are at the lower end of the allowed ranges, i.e.,  $M_c \sim 90 M_\odot$  and  $M_{\text{env}} \sim 60 M_\odot$ , may be more preferred. Additional properties that are derived include the best-fit clump mass surface density, which matches the estimates from the Herschel derived column density map (i.e.,  $0.15 \text{ g cm}^{-2}$ ). Finally, the half-opening angle of the outflow cavity,  $\theta_{\text{w,esc}} = 29^\circ \pm 10^\circ$ , is consistent with the estimate from the IR morphology seen in the JWST/NIRCam images ( $\sim 25^\circ$ ).

We see that the impact of using the half-solar-metallicity models is to slightly reduce the estimate of the current protostellar mass, while more significantly increasing the estimate of the initial core mass and current envelope mass. The impact of using the JWST fluxes (compared to the Spitzer/IRAC upper limits) is to tighten the constraints on the received flux, which impacts the isotropic bolometric luminosity,  $L_{\text{bol,iso}}$ . This yields slightly tighter constraints on parameters such as the current protostellar mass, accretion rate and age of the system.

As has been known from previous studies (e.g., R. Fedriani et al. 2023), SED fitting is prone to significant degeneracies. These are illustrated for the three primary model parameters in Figure 10. However, one of the main conclusions that can be

drawn from these distributions is that the inference of a relatively high protostellar mass, i.e., with  $m_* \sim 10 M_\odot$ , appears to be relatively robust. However, it should be noted that the models assume a single dominant source is responsible for the observed fluxes. If another protostar (such as S284p2 or the one in the core c1b) contributes to this flux significantly, e.g., at the 50% level, then the mass estimate for S284p1 would be reduced, but only by a relatively modest amount, i.e., from  $m_* = 10.2^{+3.9}_{-2.8} M_\odot$  to  $m_* = 9.1^{+2.9}_{-2.2} M_\odot$ .

On the other hand, we also attempt to assess the properties of S284p2 with SED fitting, as the source is clearly resolved in the NIRCam images. Although its flux contribution at longer wavelengths is not well constrained, our analysis suggests that S284p2 can be interpreted as an intermediate-mass protostar viewed through significant extinction (see Appendix B).

### 3.2.3. The S284p1 Outflow

To search for  $\text{H}_2$  line-emitting structures, we present the continuum-subtracted F470N image in Figure 11(a). The continuum level is estimated by extrapolation from the F356W-band flux densities. The idea is that the continuum emission in the F470N is most likely dominated by the nebulosity on larger spatial scales, while shock knots that emit

**Table 1**  
Parameters of the Average and Dispersion of “Good” Models

Case	#	$M_c$ ( $M_\odot$ )	$\Sigma_{cl}$ ( $\text{g cm}^{-2}$ )	$R_{core}$ (pc)	$m_*$ ( $M_\odot$ )	$\theta_{view}$ (deg.)	$A_V$ (mag)	$M_{env}$ ( $M_\odot$ )	$\theta_{w,esc}$ (deg.)	$\dot{m}_*$ ( $10^{-5}M_\odot \text{ yr}^{-1}$ )	$L_{bol,iso}$ ( $10^4 L_\odot$ )	$L_{bol}$ ( $10^4 L_\odot$ )	$t_{age}$ ( $10^5 \text{ yr}$ )
S284p1-case1	#79	$63^{+28}_{-19}$	$0.21^{+0.27}_{-0.12}$	$0.13^{+0.09}_{-0.05}$	$12.7^{+7.0}_{-4.5}$	$38 \pm 16$	$152 \pm 38$	$25^{+23}_{-12}$	$47 \pm 13$	$7.9^{+5.1}_{-3.1}$	$3.1^{+7.3}_{-2.2}$	$2.4^{+3.1}_{-1.4}$	$2.4^{+1.7}_{-1.0}$
S284p1-case2	#148	$107^{+35}_{-27}$	$0.11^{+0.05}_{-0.04}$	$0.23^{+0.08}_{-0.06}$	$11.7^{+7.2}_{-4.4}$	$48 \pm 21$	$147 \pm 32$	$68^{+35}_{-23}$	$34 \pm 14$	$6.3^{+1.6}_{-1.3}$	$1.7^{+3.3}_{-1.1}$	$1.9^{+2.7}_{-1.1}$	$3.2^{+1.6}_{-1.1}$
S284p1-case3	#95	$110^{+25}_{-20}$	$0.10^{+0.01}_{-0.01}$	$0.24^{+0.04}_{-0.03}$	$10.2^{+3.9}_{-2.8}$	$58 \pm 18$	$129 \pm 21$	$80^{+31}_{-23}$	$29 \pm 10$	$6.0^{+0.6}_{-0.6}$	$0.9^{+0.4}_{-0.3}$	$1.5^{+1.1}_{-0.6}$	$3.1^{+0.7}_{-0.6}$

**Note.** Columns from left to right describe the source and case of SED fitting method; number of “good” models that are able to fit the SED; initial core mass ( $M_c$ ); mass surface density of the clump environment ( $\Sigma_{cl}$ ); radius of the core ( $R_{core}$ ); current protostellar mass ( $m_*$ ); angle of the line of sight to the outflow axis ( $\theta_{view}$ ); amount of foreground extinction ( $A_V$ ); mass of the infalling envelope ( $M_{env}$ ); half-opening angle of the outflow cavity ( $\theta_{w,esc}$ ); accretion rate of the protostar ( $\dot{m}_*$ ); bolometric luminosity assuming isotropic emission of the flux ( $L_{bol,iso}$ ); true intrinsic bolometric luminosity ( $L_{bol}$ ); and age of the protostar ( $t_{age}$ ).



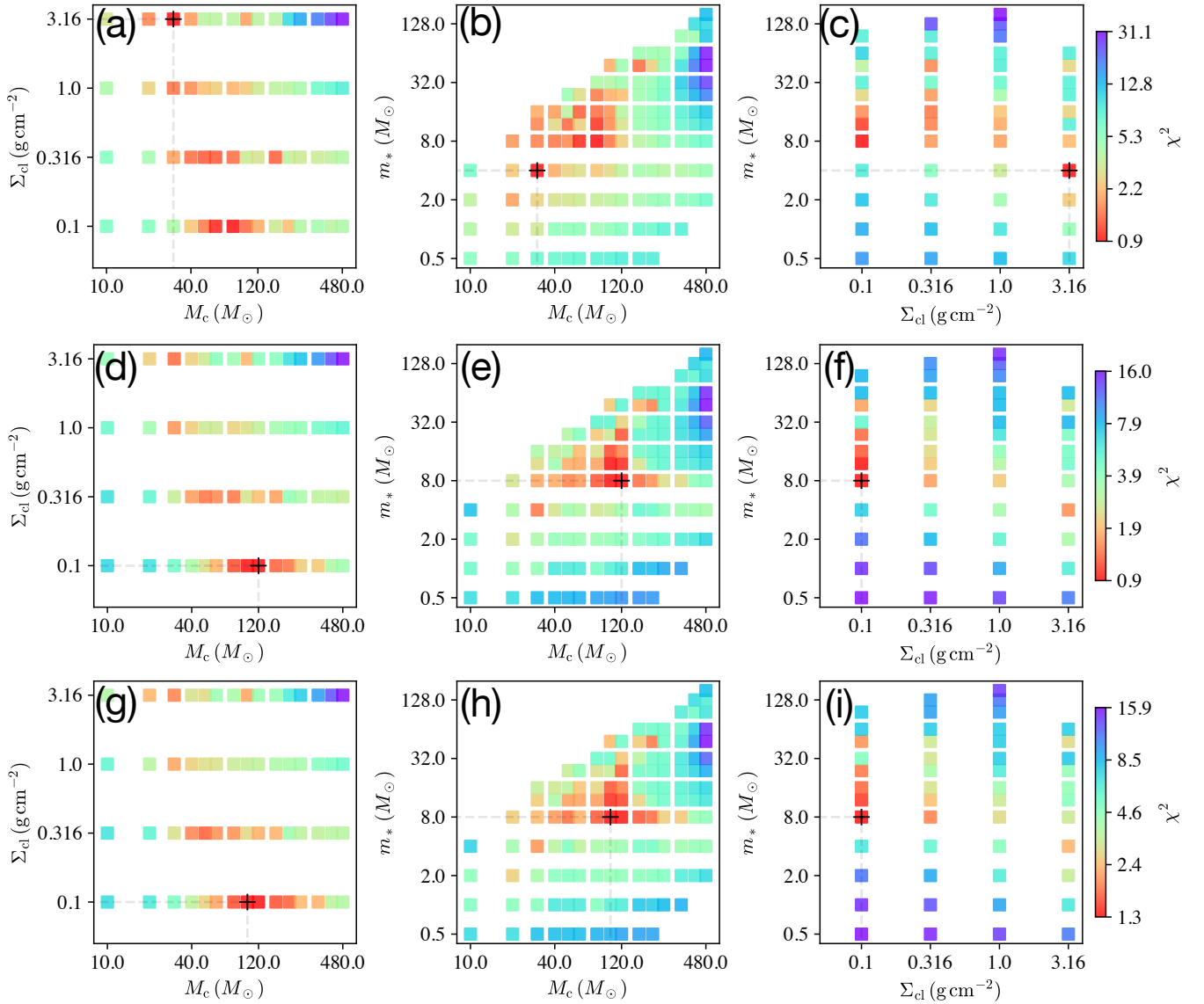


**Figure 10.** Diagrams of the reduced  $\chi^2$  distribution of SED model fitting in  $\Sigma_{\text{cl}}-M_{\text{c}}$  space,  $m_{*}-M_{\text{c}}$  space, and  $m_{*}-\Sigma_{\text{cl}}$  space. The black crosses and dashed gray lines mark the locations of the best models. The white regions are where  $\chi^2$  is larger than 50. Panels (a)–(c), (d)–(f), and (g)–(i) show the SED fit results for Cases 1, 2, and 3, respectively (see text).

H2 lines are expected to be relatively compact. To isolate such features, we first derive a ratio map for  $F(4.70 \mu\text{m})/F(3.56 \mu\text{m})$  on a pixel-by-pixel basis and smooth it with a Gaussian kernel with an FWHM of  $15''$ . We then take this smoothed ratio map as a proxy for the nebulosity continuum ratio between the two bands. We have tested different FWHM sizes and found that  $15''$  provide an optimal compromise between capturing broad-scale nebulosity and minimizing artifacts. We then multiply the F356W image by this ratio map to estimate the continuum contribution in the F470N band, which is subsequently subtracted from the original F470N image. We note that the F356W image could contain lines from H<sub>2</sub> so the  $4.70 \mu\text{m}$  line emission could potentially be somewhat oversubtracted.

From Figure 11(a) we see that the global extent of the outflow appears to be contained in the image. The furthest extent of the eastern outflow is defined by knot E1, while that of the western outflow by knot W1. With the central driving source, i.e., S284p1, identified in the JWST/F356W images located at R.A.,

decl. of  $(6^{\text{h}} 46^{\text{m}} 15.93^{\text{s}}, +0^{\circ} 6' 28''.2)$ . From this position we can draw vectors that extend to the furthest extent of the outflows seen in the image (Figure 5(b)). The morphology of the H<sub>2</sub> emission at these extremities suggests that these are collimated bow shocks associated with the outflow propagating into the ambient interstellar medium (ISM). The positions defining the end points of the outflow, i.e., the locations of E1 and W1, are not as well defined as that of S284p1. However, we set them to be  $(6^{\text{h}} 46^{\text{m}} 21.16^{\text{s}}, +0^{\circ} 6' 47''.09)$  for the NE outflow and  $(6^{\text{h}} 46^{\text{m}} 12.67^{\text{s}}, +0^{\circ} 5' 51''.11)$  for the SW outflow. Thus the position angles of the NE and SW vectors are  $66.3$  and  $232.8$ , respectively. Their linear extents in the plane of the sky are  $46''.5$  (1.01 pc) and  $61''.2$  (1.34 pc), respectively, i.e., an average length of 1.18 pc.

If E1 and W1 represent the locations of the outer bow shocks of the outflow, then we can assess the average speed that they have propagated through the ISM given the estimated age of the protostar, i.e.,  $t_{\text{age}} \sim 3 \times 10^5$  yr. In the plane of the

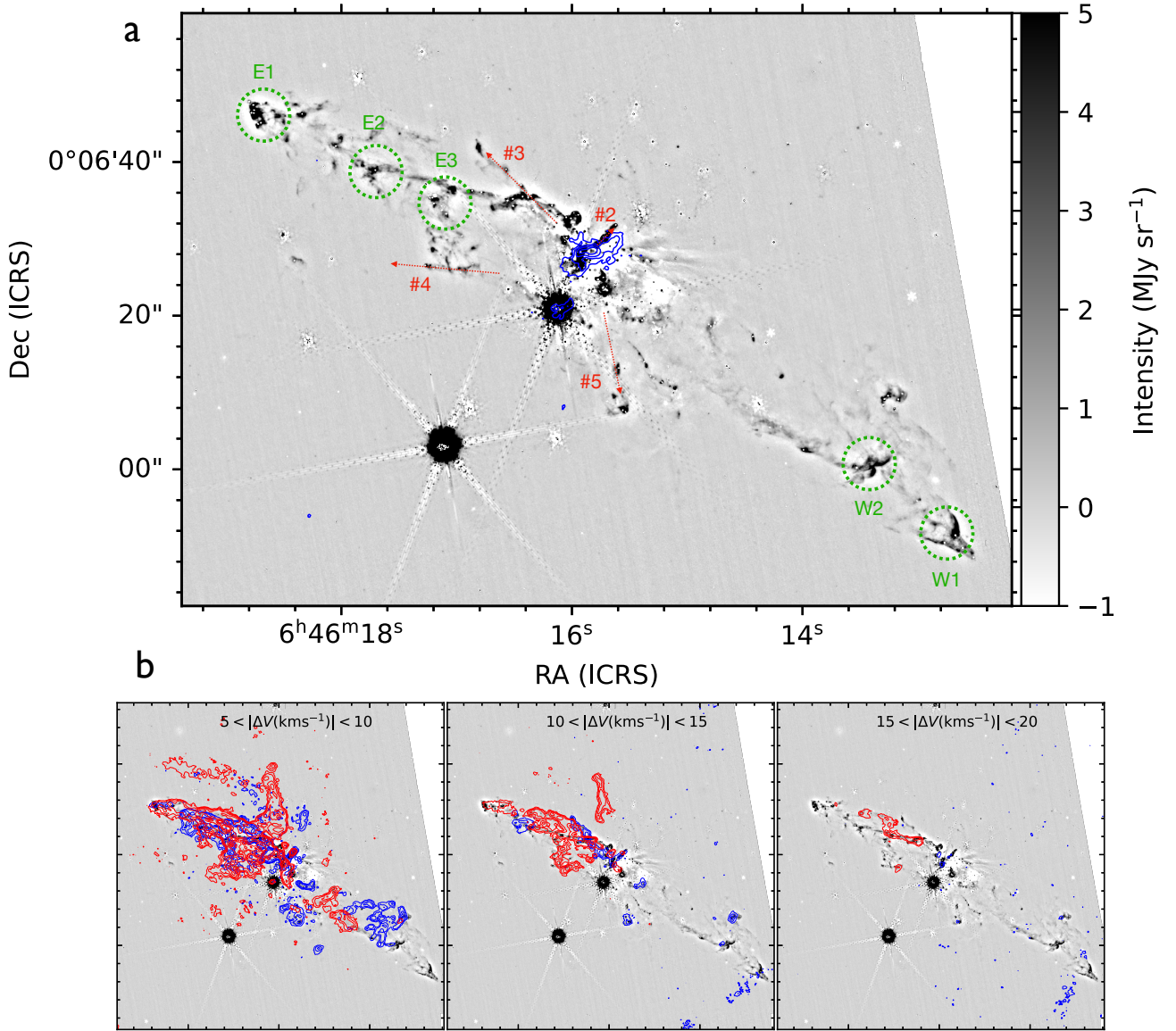


**Figure 11.** The S284p1 massive protostellar outflow seen in the H<sub>2</sub> 4.7 μm and CO(2–1) lines. (a) The F470N image after continuum subtraction. The blue contours show ALMA 1.3 mm continuum emission with contour levels of (5, 10, 20, 40, 80) × 0.11 mJy beam<sup>-1</sup>. The green circles and red arrows denote the prominent knots in the main jet and other possible jets in the region. (b) The blueshifted and redshifted CO (2–1) emission integrated in three velocity ranges from 5 to 20 km s<sup>-1</sup> relative to the systemic velocity.

sky, this average speed is 3.8 km s<sup>-1</sup>. The true 3D length and average speed of the outflow is greater than the plane-of-sky component by  $(\sin \theta_{\text{view}})^{-1}$ . The value of  $\theta_{\text{view}}$  is not very well constrained from the SED fitting, but if we adopt a value of 60°, then the 3D length and average speed are only boosted by a factor of 1.15, i.e., an implied average 3D speed of 4.4 km s<sup>-1</sup>. We note that a near plane-of-sky orientation for the outflow axis is supported by the fact that both blue- and redshifted CO emission components are seen in the eastern outflow.

The speed of the primary wind material launched in protostellar outflows is expected to increase as the mass of the protostar grows. Thus it is possible that the current extent of the outflow, as traced by E1 and W1, is driven by more recent outflow activity. For example, if the material defining E1 and W1 was launched 10<sup>5</sup> yr ago, then the average propagation speed would be 3 times greater than the above

estimates, i.e.,  $\sim 13$  km s<sup>-1</sup>. Furthermore, the current propagation speed, e.g., which may be possible to measure via future proper motion studies, would be expected to be larger than the average.

Figure 11(a) reveals other H<sub>2</sub> emission features along the outflow axis. On the western side, we identify the W2 knot complex, which, like W1, also exhibits a bow-shock-like morphology. W2’s location is about 75% of the distance to W1. On the eastern side, after E1, the next most prominent H<sub>2</sub> emission feature is the E2 complex, which also shows a bow-shock morphology. It is located about 65% of the distance to E1. It is thus possible that W2 and E2 were caused by a common event of increased level of outflow activity that occurred after the earlier outflow activity that produced W1 and E1. It is possible that such outflow activity has been driven by a relatively transient accretion “burst.” However, it could also reflect a more sustained level of faster outflow speeds.

Such an increase in outflow speed is expected as the protostar grows in mass and/or shrinks in size (e.g., J. E. Staff et al. 2023). We also note that on the eastern side, there are a greater number of other outflow knots present, including the prominent E3 complex that is interior to E2. As marked in Figure 11(a), there are also several features that may trace outflows driven by other protostars in the region.

Next we consider the outflow traced by CO(2–1) emission. Figure 11(b) presents the CO(2–1) integrated intensity map over different velocity ranges relative to the systemic velocity,  $v_{\text{sys}} = 41.2 \text{ km s}^{-1}$ , which is determined from dense gas tracers, such as  $\text{C}^{18}\text{O}(2-1)$  and  $\text{DCO}^+(3-2)$ . On the eastern side, where there is a greater level of CO emission than the western side, where the CO(2–1) emission exhibits a spatial extent similar to that of the  $\text{H}_2 4.7 \mu\text{m}$  line. The relative lack of CO emission on the western side may indicate a stronger FUV radiation field in this location, which would be consistent with a scenario of greater exposure to the radiation field from the Dolidze 25 young cluster, which is to the west of S284-FIR1. If the western molecular outflow has suffered a greater degree of photodissociation, then it should be correspondingly brighter in emission from atomic and/or ionized carbon.

Considering kinematics, as shown in Figure 11(b), most of the CO emission is present at velocity amplitudes from 5 to  $10 \text{ km s}^{-1}$  away from the systemic velocity, with smaller amounts from 10 to  $15 \text{ km s}^{-1}$  and very minor components from 15 to  $20 \text{ km s}^{-1}$ . The overlapping of blueshifted and redshifted emission in both the eastern and western lobes suggests that the global outflow orientation is close to the plane of the sky. However, if the protostellar outflow has evolved to have relatively wide angle driving at the core scale, then a large range of both blue- and redshifted gas is expected, especially in the inner regions.

We measure the integrated fluxes of the eastern outflow lobe in order to estimate its associated mass. The column densities are derived from the measured line fluxes, using the `calcu` toolkit (S. Li et al. 2020), for which local thermodynamic equilibrium conditions and optically thin line emission have been assumed. We assume a constant excitation temperature of 20 K and a  $^{12}\text{CO}$  abundance of  $0.5 \times 10^{-4}$  with respect to  $\text{H}_2$ , i.e., half the canonical abundance of solar neighborhood clouds (G. A. Blake et al. 1987). For the blueshifted component (from 30 to  $40.5 \text{ km s}^{-1}$ ) we estimate a mass of  $4.6 M_{\odot}$  (with the innermost  $1.5 \text{ km s}^{-1}$  channel contributing  $1.6 M_{\odot}$ ), while for the redshifted component (from 43.5 to  $67 \text{ km s}^{-1}$ ) we derive  $8.4 M_{\odot}$  (with the innermost channel contributing  $1.8 M_{\odot}$ ). Thus the total mass traced by CO(2–1) emission in the eastern lobe is about  $13 M_{\odot}$ . The total may be underestimated by a few solar masses, since we have excluded the innermost  $\pm 1 \text{ km s}^{-1}$  about the systemic velocity.

We can compare the above CO-traced mass with the amount of core mass swept up by outflow feedback from the best-fitting SED models (Section 3.2.2). For Case 3, the half-opening angle of the outflow cavity is estimated to be  $\theta_{\text{w,esc}} = 32^\circ$ . Thus the fraction of one hemisphere of the initial core mass that is swept up by one outflow cavity is  $1 - \cos \theta_{\text{w,esc}} \rightarrow 0.15$  (assuming a spherical core). For the best-fit initial core mass of  $110 M_{\odot}$ , this implies a swept-up mass of  $\sim 9 M_{\odot}$ . Although the systematic uncertainties are at a level of at least a factor of 2, the approximate agreement between the observed and theoretical mass estimates of the

outflow lobe suggests further support for the core accretion model.

While observations of outflow momentum fluxes can, in principle, constrain protostellar models (see, e.g., D. Xu et al. 2024), this becomes highly uncertain when the orientation of the system is close to the plane of the sky, i.e., since only a small part of the momentum flux is traced by line-of-sight motions. Thus, we do not attempt here to measure the momentum flux of the outflow. We note that the maximum observed CO(2–1) velocities from a beam-sized extracted spectrum of S284p1 are about  $15 \text{ km s}^{-1}$  from the systemic velocity of the core. Such maximum observed velocities can, in principle, be used to help constrain the inclination angles and other properties of core accretion models.

### 3.2.4. Implications of the S284p1 Outflow Geometry for Massive Star Formation Theories

Here we consider the observed global geometry of the outflow from S284p1 and the implications for massive star formation theories. As discussed, Figure 5(b) shows annotations that indicate the geometry of the two sides of the outflow. We see that the S284p1 outflow exhibits a high degree of symmetry. The end points of the two sides (E1 and W1 knots shown in Figure 11(a)) are well aligned with a common axis, i.e., their angular offset from a common axis is in total only  $13.5^\circ$ , or  $\lesssim 7^\circ$  for each side of the outflow. Similarly, the total plane-of-sky-projected outflow lengths are very similar, i.e., each deviates from the average length of  $1.18 \text{ pc}$  by  $\lesssim 15\%$ . Variations in the density of the ambient ISM on either side of S284p1, as well as jet precession, could lead to such differences in outflow directions or extensions. Another optional scenario is that if S284p1 has a plane-of-sky motion in a direction perpendicular to the outflow axis that differs from that of the initially launched gas, then this could lead to the observed level of misalignment. Such motion could result from acceleration acquired by S284p1 during the course of its formation.

To evaluate the level of acceleration that is required, we adopt an estimate of the protostellar age based on SED fitting (Section 3.2.2) of  $t_{\text{age}} \sim 3 \times 10^5 \text{ yr}$ . If S284p1 started forming at a location that was perfectly aligned with the observed axis connecting the two outflow bow shocks, then it has moved by a projected distance of about  $0.14 \text{ pc}$  in the plane of the sky. The magnitude of (constant) acceleration needed to achieve this displacement over the course of  $3 \times 10^5 \text{ yr}$  is  $a \sim 10^{-8} \text{ cm s}^{-2}$  (leading to a current plane-of-sky motion of about  $1 \text{ km s}^{-1}$ ). However, the current observed bow shocks were most likely launched more recently, when the protostar was already relatively massive, i.e., the current observed outflow timescale should be  $t_{\text{outflow}} < t_{\text{age}}$ . For example, adopting  $t_{\text{outflow}} \sim 10^5 \text{ yr}$  then requires  $a \sim 9 \times 10^{-8} \text{ cm s}^{-2}$  and a current plane-of-sky motion of  $2.7 \text{ km s}^{-1}$ .

The most likely cause of acceleration for S284p1 is gravitational infall toward the core c1b, with the resulting direction of motion being consistent with this scenario. In addition, the expected magnitude of this acceleration is  $a_{\text{c1b}} = 7 \times 10^{-8} (M_{\text{c1b}}/50 M_{\odot})(d/0.1 \text{ pc})^{-2} \text{ cm s}^{-2}$ . Thus, while these estimates are quite uncertain, to an order of magnitude the amplitude and direction of acceleration due to gravitational infall toward c1b could explain the apparent offset of S284p1's current location from the outflow axis defined by the pair of outer bow shocks.



Regardless of whether S284p1 has suffered recent acceleration at the above levels, to first order the global outflow morphology is very symmetric. The main conclusion that can be drawn from this symmetry is that the protostar has held a steady orientation over the lifetime of the observed outflow, i.e., especially of its inner disk, which is expected to launch the fastest part of the outflow. Such a stable orientation is most naturally expected in core accretion models (e.g., C. F. McKee & J. C. Tan 2003), in which the disk is fed by the collapse of a relatively symmetric core-infalling envelope. In contrast, in competitive accretion models (e.g., I. A. Bonnell et al. 2001; M. Y. Grudić et al. 2022) the accretion (and thus outflow) history is expected to be much more disordered leading to significant changes in outflow orientation. The observational constraints presented above on the degree of symmetry of oppositely directed outflow bow shocks from a massive protostar motivate the need for quantitative measures of this property as tests of numerical simulations of massive star formation. We note that the reason why certain numerical simulations of massive star and star cluster formation often show evidence of competitive accretion is likely to be due to initial conditions that do not include regions of dynamically important magnetic fields (see, e.g., M. J. Butler & J. C. Tan 2012; J. C. Tan et al. 2014; C.-Y. Law et al. 2024).

#### 4. Discussion

Massive stars ( $\gtrsim 10 M_{\odot}$ ) have a major impact on their surroundings via their radiative, mechanical, and chemical feedback. Despite this importance, the mechanisms of their formation and how these may vary with environmental conditions remain subjects of intense investigation (J. C. Tan et al. 2014). Theoretical models predict substantial dependencies on metallicity in the formation, feedback, evolution, and end products of massive stars (e.g., K. E. I. Tanaka et al. 2018), but direct observations rarely probe down to the immediate surroundings of individual YSOs at a few thousand astronomical unit scales due to their typical large distances. The best characterized case to date, HH 1177 in the LMC, is found to be a massive protostar system with a collimated jet and rotating toroid (A. F. McLeod et al. 2018, 2024), which is consistent with the canonical disk-mediated star formation picture. However, HH 1177 is relatively isolated. Furthermore, it is an optically revealed source that has evacuated most of its natal material and is thus likely to have evolved beyond its main accretion phase.

In contrast to HH 1177, S284p1 is deeply embedded in its natal material and is actively accreting, thus providing an opportunity to examine low-metallicity massive star formation at an early stage. S284p1 is also seen to be forming in a clustered environment, i.e., surrounded by hundreds of lower-mass YSOs, as well as several other lower-mass protostars driving relatively small jets. In addition, being at a much closer distance, allows the resolution of much smaller spatial scales in the case of S284p1 compared to HH 1177.

In this paper, the first of the LZ-STAR survey, we have focused on a detailed, quantitative study of the properties of the most massive protostar in the region, S284p1. We have argued that its highly symmetric outflow morphology is strong evidence for an “ordered” formation history, consistent with the simplest expectations of core accretion models. We have developed new massive protostar RT models designed for the low-metallicity (half-solar) conditions of the S284 region.

Fitting these models to the NIR to FIR SED of S284p1 yields estimates of the current protostellar mass of about  $10 M_{\odot}$ , with a current age of  $\sim 3 \times 10^5$  yr. We have explored the degeneracies in protostellar properties that arise from SED fitting. While SED fitting results are quite uncertain, several other pieces of evidence provide quantitative support to the derived model. These include the JWST/NIRCam-observed NIR outflow cavity, which aligns with the global outflow axis and has a half-opening angle that is broadly consistent with that derived from SED fitting. In addition, the amount of CO-traced mass in the outflow lobe is consistent with the material expected to have been ejected from the natal core by the action of outflow feedback.

We note that some qualitative features of the star formation activity in S284 based on the public ALMA and JWST data of the LZ-STAR survey have been presented by O. R. Jadhav et al. (2025), however this study, which we have only become aware of in the final stages of the preparation of our paper, is not part of the LZ-STAR survey and has not influenced our analysis.

For a better understanding of the massive protostar S284p1, higher angular resolution ALMA observations are needed to better probe its accretion disk, especially to see if its current orientation aligns orthogonally to the outflow axis. Observations of disk kinematics could also yield a dynamical estimate of the current protostellar mass that can be compared to the SED-derived value. JWST spectroscopic studies of the protostar and its outflow (see, e.g., H. Beuther et al. 2023, for an example of such observations) should yield improved kinematic constraints on the theoretical models, as well as probing ice absorption features in the infalling envelope. Finally, a second epoch NIRCam observation is needed to constrain proper motion kinematics of the outflow features.

#### 5. Conclusion

We have undertaken a multiwavelength survey in the outer Galaxy star formation region S284 (LZ-STAR survey). As first paper of the series, we present ALMA and JWST observations of one of the most active star-forming sites in S284, S284-FIR1. Key conclusions from our study are as follows.

1. ALMA 1.3 mm continuum observations reveal a population of 22 dense cores with masses ranging from  $\sim 0.37 M_{\odot}$  to  $\sim 68 M_{\odot}$ . A subset of these cores drive CO outflows, indicating active ongoing star formation.
2. The JWST/NIRCam images reveal the presence of a nascent star cluster of about 200 detected members, whose detailed properties are the focus of the next paper in this series. A spectacular bipolar outflow traced by  $H_2(0-0 S(9))$  emission is seen to be launched from a protostar near the center of the cluster (in projection). The outflow spans a total length of 2.6 pc on the sky and is also clearly seen in CO(2–1) emission, with the kinematics indicating an orientation near that of the plane of the sky.
3. ALMA observations reveal that the dense core hosting S284p1 (c1) is fragmented into two subcores, with S284p1 residing in the  $\sim 20 M_{\odot}$  component c1a. The JWST/NIRCam F356W image reveals S284p1 as a point source surrounded by a well-defined, cone-shaped NIR cavity.

4. We have developed RT models of massive protostars designed for the low metallicity of S284 and the resulting SED analysis yields a current protostellar mass of  $\sim 10_{-3}^{+4} M_{\odot}$ , which has been forming for last  $\sim 3 \times 10^5$  yr.
5. The symmetric, bipolar outflow observed in both CO and H<sub>2</sub> emission suggests that S284p1 has undergone a stable, disk-mediated accretion over its formation history that is consistent with basic expectations of core accretion models.

### Acknowledgments

This paper makes use of the following ALMA data: ADS/JAO.ALMA#2021.1.01706.S. ALMA is a partnership of ESO (representing its member states), NSF (USA), and NINS (Japan), together with NRC (Canada), MOST and ASIAA (Taiwan), and KASI (Republic of Korea), in cooperation with the Republic of Chile. The Joint ALMA Observatory is operated by ESO, AUI/NRAO, and NAOJ. The National Radio Astronomy Observatory is a facility of the National Science Foundation operated under cooperative agreement by Associated Universities, Inc. Y.C. was partially supported by a Grant-in-Aid for Scientific Research (KAKENHI number JP24K17103) of the JSPS. J.C.T. acknowledges support from NSF grant AST-2206450 and ERC Advanced grant 788829 (MSTAR). R.F. acknowledges financial support from the Severo Ochoa grant CEX2021-001131-S, MICIU/AEI/doi:10.13039/501100011033, and PID2023-146295NB-I00.

The US-based team members acknowledge support from JWST grant GO-02317.

*Facilities:* JWST (NIRCam), ALMA.

*Software:* CASA (J. P. McMullin et al. 2007), APLpy (T. Robitaille & E. Bressert 2012), Astropy (Astropy Collaboration et al. 2013, 2018, 2022).

### Appendix A

#### Local Continuum Subtraction for JWST Narrow Bands F405N and F470N

In the narrowband F405N and F470N images, significant emission enhancement is clearly visible around the protostar, although the cone morphology is less distinct. To identify potential line-emitting structures near the protostar (S284p1), we performed continuum subtraction. This is done in a way similar to that described above for F470N on larger scales, i.e., the narrow filter images are subtracted by extrapolating the F356W image to estimate the continuum fluxes. Since we focus on the localized region centered on S284p1, we estimate the continuum flux ratio for  $F(4.05 \mu\text{m})/F(3.56 \mu\text{m})$  (or  $F(4.70 \mu\text{m})/F(3.56 \mu\text{m})$ ) with that empirically derived for a region within an aperture of  $3''$ , which is presumably dominated by diffuse nebular emission. The resulting continuum-subtracted images are shown in Figure A1. Some residual emission is seen near S284p1, but it is currently unclear if it originates from excess line emission or potential curvature of the continuum SED.

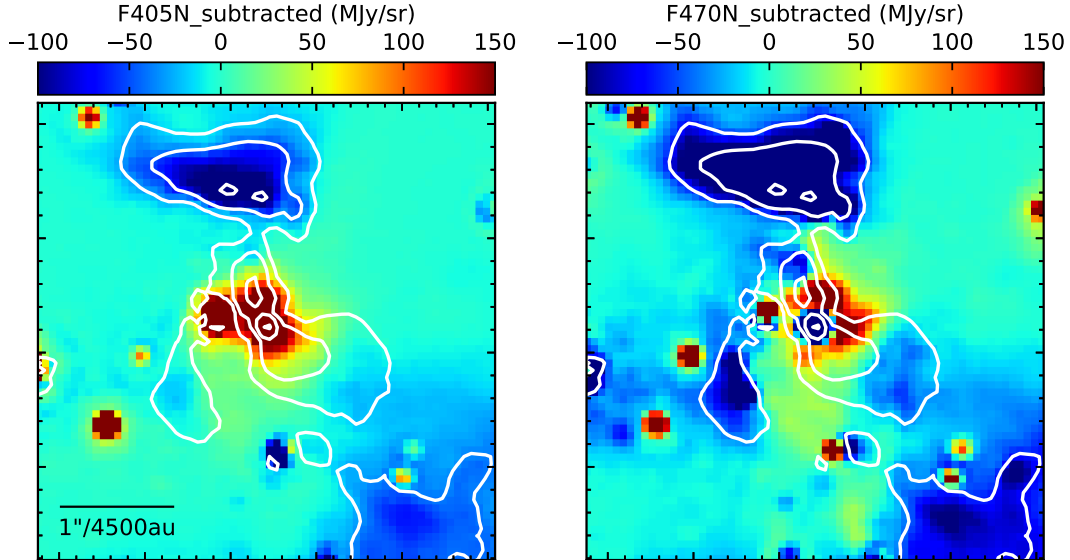


**Figure A1** Continuum-subtracted image in F405N and F470N of the surroundings of S284p1. Left: continuum-subtracted F405N image. The contours show the F356W image with levels of (50, 100, 200, and 400)  $\times$  MJy sr<sup>-1</sup>. Right: same as the left panel but for F470N.

## Appendix B

### The Spectral Energy Distribution Fit for S284p2

S284p2 is resolved in the NIRCcam images, so we are able to place some constraints its source properties from SED fitting. Figure B1 and Table B1 present the SED fitting results for S284p2. Located at a distance of  $\approx 0''.6$  from S284p1, it is challenging to separate the flux densities of the two sources at most wavelengths, except for the JWST bands. Since S284p1 is most likely the dominant source in the region, we adopt the same flux measurements as S284p1 but treat them as upper limits for S284p2. For the JWST bands, where S284p2 is

clearly detected, we measure its flux densities using a smaller aperture ( $1''$ ) and use these measurements in the SED fitting. The SED fitting results show that a wide range of parameter combinations can reproduce the observed data (owing to the many upper limit measurements). The best-fit solutions suggest that S284p2 can be explained as an intermediate-mass protostar seen through significant extinction. Since it is likely that most of the bolometric flux comes from S284p1, these estimated protostellar properties for S284p2 should mostly be regarded as upper limits, e.g., on the current protostellar mass.

**Table B1**  
Parameters of the Average and Dispersion of “Good” Models for S284p2

Case	#	$M_c$ ( $M_\odot$ )	$\Sigma_{cl}$ ( $\text{g cm}^{-2}$ )	$R_{core}$ (pc)	$m_*$ ( $M_\odot$ )	$\theta_{view}$ (deg.)	$A_V$ (mag)	$M_{env}$ ( $M_\odot$ )	$\theta_{w,esc}$ (deg.)	$\dot{m}_*$ ( $10^{-5} M_\odot \text{ yr}^{-1}$ )	$L_{bol,iso}$ ( $10^4 L_\odot$ )	$L_{bol}$ ( $10^4 L_\odot$ )	$t_{age}$ ( $10^5 \text{ yr}$ )
S284p2	#5896	$75^{+110}_{-45}$	$0.41^{+0.97}_{-0.29}$	$0.10^{+0.14}_{-0.06}$	$4.4^{+11.6}_{-3.2}$	$58 \pm 21$	$469 \pm 278$	$47^{+114}_{-33}$	$26 \pm 20$	$9.8^{+19.8}_{-6.6}$	$0.3^{+2.6}_{-0.3}$	$0.5^{+4.2}_{-0.4}$	$0.8^{+1.4}_{-0.5}$

**Note.** Columns from left to right describe the source and case of the SED fitting method; number of “good” models that are able to fit the SED; initial core mass ( $M_c$ ); mass surface density of the clump environment ( $\Sigma_{cl}$ ); radius of the core ( $R_{core}$ ); current protostellar mass ( $m_*$ ); angle of the line of sight to the outflow axis ( $\theta_{view}$ ); amount of foreground extinction ( $A_V$ ); mass of the infalling envelope ( $M_{env}$ ); half-opening angle of the outflow cavity ( $\theta_{w,esc}$ ); accretion rate of the protostar ( $\dot{m}_*$ ); bolometric luminosity assuming isotropic emission of the flux ( $L_{bol,iso}$ ); true intrinsic bolometric luminosity ( $L_{bol}$ ); and age of the protostar ( $t_{age}$ ).

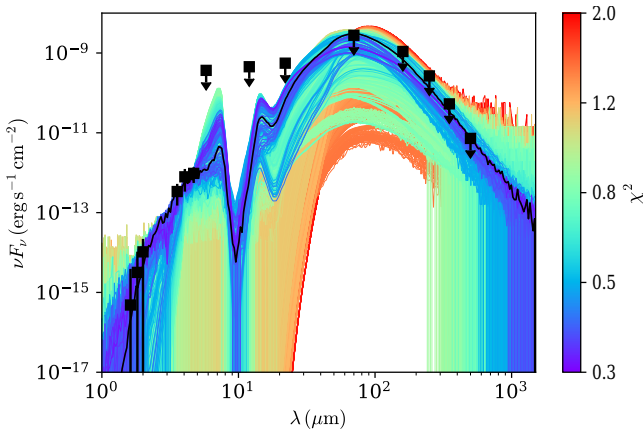


**Figure B1** SED fitting results for S284p2. The best-fitting protostar model is shown with a black line, while all other “good” model fits (see text) are shown with colored lines (red to blue with increasing  $\chi^2$ ).

### ORCID iDs

Yu Cheng <https://orcid.org/0000-0002-8691-4588>  
 Jonathan C. Tan <https://orcid.org/0000-0002-3389-9142>  
 Morten Andersen <https://orcid.org/0000-0002-5306-4089>  
 Rubén Fedriani <https://orcid.org/0000-0003-4040-4934>  
 Yichen Zhang <https://orcid.org/0000-0001-7511-0034>  
 Massimo Robberto <https://orcid.org/0000-0002-9573-3199>  
 Zhi-Yun Li <https://orcid.org/0000-0002-7402-6487>  
 Kei E. I. Tanaka <https://orcid.org/0000-0002-6907-0926>

### References

- Astropy Collaboration, Price-Whelan, A. M., Lim, P. L., et al. 2022, *ApJ*, **935**, 167
- Astropy Collaboration, Price-Whelan, A. M., Sipőcz, B. M., et al. 2018, *AJ*, **156**, 123
- Astropy Collaboration, Robitaille, T. P., Tollerud, E. J., et al. 2013, *A&A*, **558**, A33
- Bally, J. 2016, *ARA&A*, **54**, 491
- Beichman, C. A., Rieke, M., Eisenstein, D., et al. 2012, *Proc. SPIE*, **8442**, 84422N
- Beuther, H., van Dishoeck, E. F., Tychoniec, L., et al. 2023, *A&A*, **673**, A121
- Blake, G. A., Sutton, E. C., Masson, C. R., & Phillips, T. G. 1987, *ApJ*, **315**, 621
- Bonnell, I. A., Bate, M. R., Clarke, C. J., & Pringle, J. E. 2001, *MNRAS*, **323**, 785
- Bushouse, H., Eisenhamer, J., Dencheva, N., et al. 2023, JWST Calibration Pipeline, v1.12.5, Zenodo, doi:10.5281/zenodo.10022973
- Butler, M. J., & Tan, J. C. 2012, *ApJ*, **754**, 5
- Cheng, Y., Tan, J. C., Liu, M., et al. 2018, *ApJ*, **853**, 160
- De Buizer, J. M., Liu, M., Tan, J. C., et al. 2017, *ApJ*, **843**, 33
- De Marchi, G., Giardino, G., Biazzo, K., et al. 2024, *ApJ*, **977**, 214
- Draine, B. T. 2011, *Physics of the Interstellar and Intergalactic Medium* (Princeton, NJ: Princeton Univ. Press)
- Federman, S. A., Megeath, S. T., Rubinstein, A. E., et al. 2024, *ApJ*, **966**, 41
- Fedriani, R., Tan, J. C., Telkamp, Z., et al. 2023, *ApJ*, **942**, 7
- Fukui, Y., Harada, R., Tokuda, K., et al. 2015, *ApJL*, **807**, L4
- Grudić, M. Y., Guszejnov, D., Offner, S. S. R., et al. 2022, *MNRAS*, **512**, 216
- Guarcello, M. G., Biazzo, K., Drake, J. J., et al. 2021, *A&A*, **650**, A157
- Jadhav, O. R., Dewangan, L. K., Verma, A., et al. 2025, *ApJ*, **980**, 133
- Jones, O. C., Nally, C., Habel, N., et al. 2023, *NatAs*, **7**, 694
- Kinman, A. V. I., Petkova, M. A., Tan, J. C., Cosentino, G., & Cheng, Y. 2025, *ApJ*, **982**, 174
- Law, C.-Y., Tan, J. C., Skafidis, R., et al. 2024, *ApJ*, **967**, 157
- Li, J., Liu, C., Zhang, Z.-Y., et al. 2023, *Natur*, **613**, 460
- Li, S., Sanhueza, P., Zhang, Q., et al. 2020, *ApJ*, **903**, 119
- Liu, M., Tan, J. C., Cheng, Y., & Kong, S. 2018, *ApJ*, **862**, 105
- Liu, M., Tan, J. C., De Buizer, J. M., et al. 2019, *ApJ*, **874**, 16
- Liu, M., Tan, J. C., De Buizer, J. M., et al. 2020, *ApJ*, **904**, 75
- Marks, M., Kroupa, P., Dabringhausen, J., & Pawłowski, M. S. 2012, *MNRAS*, **422**, 2246
- McKee, C. F., & Tan, J. C. 2003, *ApJ*, **585**, 850
- McLeod, A. F., Klaassen, P. D., Reiter, M., et al. 2024, *Natur*, **625**, 55
- McLeod, A. F., Reiter, M., Kuiper, R., Klaassen, P. D., & Evans, C. J. 2018, *Natur*, **554**, 334
- McMullin, J. P., Waters, B., Schiebel, D., Young, W., & Golap, K. 2007, in ASP Conf. Ser. 376, *Astronomical Data Analysis Software and Systems XVI*, ed. R. A. Shaw, F. Hill, & D. J. Bell (San Francisco, CA: ASP), **127**
- Molinari, S., Swinyard, B., Bally, J., et al. 2010, *PASP*, **122**, 314
- Negueruela, I., Simón-Díaz, S., Lorenzo, J., Castro, N., & Herrero, A. 2015, *A&A*, **584**, A77
- O’Neill, T. J., Cosentino, G., Tan, J. C., Cheng, Y., & Liu, M. 2021, *ApJ*, **916**, 45
- Ossenkopf, V., & Henning, T. 1994, *A&A*, **291**, 943
- Puga, E., Hony, S., Neiner, C., et al. 2009, *A&A*, **503**, 107
- Rieke, M. J., Kelly, D., & Horner, S. 2005, *Proc. SPIE*, **5904**, 1
- Robitaille, T., & Bressert, E., 2012 APLpy: Astronomical Plotting Library in Python, Astrophysics Source Code Library, ascl:1208.017
- Rosolowsky, E. W., Pineda, J. E., Kauffmann, J., & Goodman, A. A. 2008, *ApJ*, **679**, 1338
- Sharpless, S. 1959, *ApJS*, **4**, 257
- Shimonishi, T., Das, A., Sakai, N., et al. 2020, *ApJ*, **891**, 164
- Shimonishi, T., Izumi, N., Furuya, K., & Yasui, C. 2021, *ApJ*, **922**, 206
- Shimonishi, T., Onaka, T., Kawamura, A., & Aikawa, Y. 2016, *ApJ*, **827**, 72
- Shimonishi, T., Tanaka, K. E. I., Zhang, Y., & Furuya, K. 2023, *ApJL*, **946**, L41
- Staff, J. E., Tanaka, K. E. I., Ramsey, J. P., Zhang, Y., & Tan, J. C. 2023, *ApJ*, **947**, 40
- Tan, J. C., Beltrán, M. T., Caselli, J. P., et al. 2014, in *Protostars and Planets VI*, ed. H. Beuther et al. (Tucson, AZ: Univ. Arizona Press), **149**
- Tanaka, K. E. I., Tan, J. C., Zhang, Y., & Hosokawa, T. 2018, *ApJ*, **861**, 68
- Telkamp, Z., Fedriani, R., Tan, J. C., et al. 2025, *ApJ*, **986**, 15
- Tokuda, K., Harada, N., Tanaka, K. E. I., et al. 2023, *ApJ*, **955**, 52
- Tokuda, K., Kunitoshi, Y., Zahorecz, S., et al. 2025, *ApJ*, **980**, 269
- Tokuda, K., Zahorecz, S., Kunitoshi, Y., et al. 2022, *ApJL*, **936**, L6
- Turner, J., Kirby-Docken, K., & Dalgarno, A. 1977, *ApJS*, **35**, 281
- Xu, D., Tan, J. C., Staff, J. E., et al. 2024, *ApJ*, **966**, 117
- Yasui, C., Izumi, N., Saito, M., et al. 2024, *ApJ*, **975**, 152
- Yasui, C., Kobayashi, N., Tokunaga, A. T., Terada, H., & Saito, M. 2006, *ApJ*, **649**, 753
- Zhang, Y., & Tan, J. C. 2018, *ApJ*, **853**, 18